Additive Manufacturing of High Temperature Strain Gauges

by

Jeremy Vandenberg

A thesis
presented to the University of Waterloo
in fulfilment of the
thesis requirement for the degree of
Master of Applied Science
In
Chemical Engineering

Waterloo, Ontario, Canada, 2018

Author's Declaration

I hereby declare that I am the sole author of this thesis. This is a true copy of the thesis, including any required final revisions, as accepted by my examiners.

I understand that my thesis may be made electronically available to the public.

Statement of Contributions

Dr. Ehsan Marzbanrad has contributed to this work by establishing the initial chemical reduction technique first screened in this work. He has also imaged by SEM the images here provided. He has also provided the mentorship and practical guidance that has enabled this work.

Dr. Paola Russo aided by providing the Raman Spectroscopy tests here included.

Shirin Khanna aided and carried out some of the printing and synthesis steps as part of a co-op program.

All other experimental design, analysis, and writing are my own or are reused under copyright permission and license.

Abstract

Additive manufacturing (AM) is quickly leading a new revolution in manufacturing. Aerosol ink jet printing (AJP) is a non-contact printing method that allows for printing on irregular substrates. When paired nanoparticulate ink, the method can print electrical traces and sensors. AJP stands to surpass current thin film technologies by flexibly printing on complex geometries. This thesis details the preliminary work towards employing AJP to create sensors operating in harsh environments. Specifically, the development of materials required to enable printed circuits functioning at temperatures exceeding 1000˚C (1850 ˚F).

The high temperature corrosion behavior of devices created from nanoparticles is explored from starting with the synthesis of the nanoparticles themselves. Inks suitable for AJP are formed from the nanoparticles. The inks are subsequently printed into strain gauge designs, sintered to bulk, and tested for conductivity. A technique to create core shell nanoparticles is demonstrated in efforts to make the ink materials more resistant to side reactions during the sintering phase.

An additional design aspect is introduced in the form of sol gels to solve the corrosion challenges presented. Sol gels were developed to create ceramic thin films to insulate the manufactured sensors, provide an engineered surface, and encapsulation layer for the devices. Sol gel chemistry is a wet chemical approach for forming ceramics that is also found to be compatible with AJP processes.

Only a few sensors produced were suitable for electrical characterization. This was due to side reactions in the sintering process as well as insufficient adhesion of the printed traces to the substrate. The resistive path of the sensor was 31 kohms, which was outside of the testing range

for strain gauges. The elevated resistance of these samples is due to impurities and defects in the printed patterns.

The findings of this thesis are useful for generating the next generation devices for use in harsh environments. The materials established here can be altered by differing processing techniques to eliminate the barriers to achieving integrated strain gauges by additive manufacturing.

Acknowledgements

I'd like to thank firstly GE Aviation for their funding and support alongside the University of Waterloo and the National Sciences and Engineering Research Council of Canada. Particular thanks go to Martin Beaumier and Louis Lefebvre at GE Aviation.

I would also like to acknowledge the research team, Dr. Ehsan Marzbanrad, Dr. Elahe Jabari, Francis Dibia, and Dr. Paola Russo for their support and encouragement throughout.

I was also supported by a friendly and welcoming research group, Aleksander Cholewinski, Kuo Yang, Dr. Geoff Rivers, Dr. Hamed Shashsavan, and Kelvin Liew for excellent discussions and lab assistance.

Lastly I'd like to thank my supervisors, Dr. Boxin Zhao and Dr. Ehsan Toyserkani, without whom this project would not be possible. Your patience and correction have helped me become a better professional and individual. Thank you for setting up your research groups and labs to facilitate this research.

Dedication

I`d like to dedicate this work to those who have helped and befriended me along the way: my parents for their mentorship and patience, my church family for helping me grow, and God who is the source of all knowledge and has left His world for us to discover.

Table of Contents

Table of Figures

List of Abbreviations

AJP	Aerosol Inkjet Printing
NiCr	Nickel Chromium Alloys
PdCr	Palladium Chromium Alloys
PdCr13	Palladium Chromium alloy with 13% by weight Chromium.
NASA	National Aeronautics and Space Administration
STEM	Scanning Tunneling Electron Microscope
BCC	Body Centered Cubic
PVP	Polyvinylpyrrolidone
TMOS	Tetramethylorthosilicate
TEOS	Tetraethylorthosilicate

List of Symbols

ε	Strain
L	Length
σ	Stress
E	Young's Modulus
γ	Gauge factor
R	Resistance
Ω	Ohms
T	Temperature
CTE	Coefficient of Thermal Expansion
CTR	Coefficient of Thermal Resistance
KE	Kinetic Energy
M	Mass
a	Amplitude
ω	Frequency
S	Cross Sectional Scattering Area
μ_T	Thermal mobility
τ_T	Mean Free Scattering Time

ρ	Resistance
G	Gibb's Free Energy
$G°$	Standard Gibb's Free Energy
R_g	Gas Constant
Q_r	Reaction Quotient
E_{cell}	Cell Potential
F	Faraday's Constant
d	Diameter
c_1	Experimental Factor
σ_l	Surface Tension
ρ_d	Density
V	Flow Velocity
Re	Reynolds Number
R_{tip}	Radius of Tip
χ	Gas Flow Ratio
η	Dynamic Viscosity
U	Droplet Velocity
C_c	Cunningham Correction Factor

$H_{p,m}$	Hamaker Constant
U	Potential Energy
G_f	Strain Energy Release Rate
h_c	Critical height

Quote

"And now here is my secret, a very simple secret: It is only with the heart that one can see rightly; what is essential is invisible to the eye."

Antoine de Saint Exupéry in *The Little Prince*

1 Introduction

This thesis will concern itself with high temperature strain gauges produced by aerosol inkjet printing (AJP). AJP is a developing form of additive manufacturing[1]–[3]. The goal of additive manufacturing is to create manufactured goods directly from the joining of micron or nano sized particles. This thesis covers diverse areas in material science from metal and ceramic nanomaterials, corrosion, and electronic materials. The work presented facilitates a new manufacturing process where nanotechnology and additive manufacturing meet.

To make strain gauges the conventional approach is to use a physical deposition method. In physical deposition the metal vapours are condensed onto the substrate after being patterned on the substrate by masking or lithography [4]. The physical deposition method is limited to only planer surfaces and by the expensive patterning processes. In contrast, additive manufacturing can be employed to make the process cheaper, more flexible, and apply to non-planar surfaces. Additive manufacturing of printed circuit components traditionally employs ink jet printing. In inkjet printing materials are suspended in jettable inks. Reservoirs of inks are processed by microfluidics into micron sized droplets and impacted on the substrate underneath. The typical distance from printer head to substrate must be less than 2mm [2]. The APJ process resolves this limitation and gives a focal depth of printing of 5mm allowing metallic patterns to be applied to complex geometries.

AJP operates by printing a continuous stream of ink in the form of aerosolized droplets. These aerosolized droplets can be focused into a pattern as seen in Figure 1. Aerosol ink jet printing can focus the stream of ink into narrower feature sizes than is capable with ink jet printing. As well

the aerosolization process is less sensitive to viscosity and surface tension of the ink than the jetting process. As such a wider range from 0.5 to 5000 cP can be printed with the machine. The printer has great focal depth of printing due to the laminar flows of pressurized air that serves as the carrier for the aerosolized inks. All these combinations make aerosol additive manufacturing an attractive method for printing on large scale non-planar and flexible parts [1], [5].

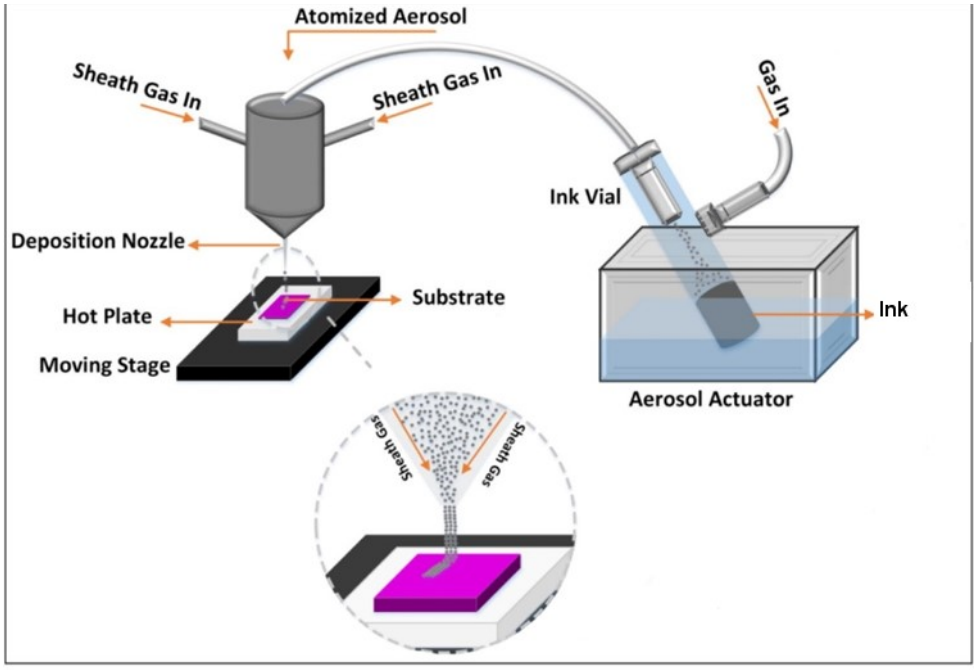

Figure 1 Aerosol Ink Jet Process [5]

The current method to make strain gauges for high temperature applications is by physical vapour deposition (PVD) techniques such as sputtering. PVD involves patterning by lithography or masking technologies that involve many process steps and can only reliably pattern on flat surfaces. Figure 2 illustrates the reduction in process steps between PVD and additive manufacturing, also termed direct write, technologies. Masking technologies require that the mask be near the substrate. The gap distance is typically 50 μm. This short distance prevents curved and complex shapes from being directly patterned.

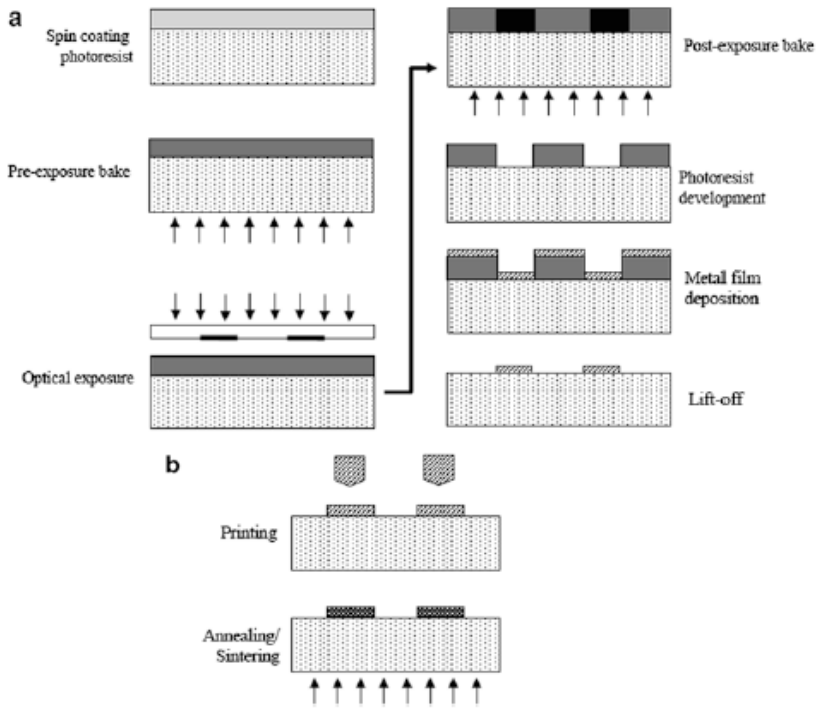

Figure 2 Comparison of strain gauges technologies: a) steps involved in traditional PVD deposition of strain gauges b) Process steps involved in additive manufacturing of strain gauges

The current limitation of the AJP process is that there exists a restricted selection of inks for the AJP process. We aim to extend the usage of aerosol ink-jet printing into specialty alloyed components. The goal set out by this project is to initialize the development of the inks from synthesis to processing; expanding the applications for the AJP process.

The area of interest for expansion is high temperature metal alloys. These alloys typically are a blend of transition metal elements and noble metals. A typical ink that can be utilized in an aerosol ink jet process contains nanoparticles of the metal components suspended in a matrix of solvents and additives. The blends allow novel additively manufactured strain gauges.

New technologies have been pushing the limits of both the temperatures and rotational speeds of turbines [6], [7]. Additive manufactured strain gauges are expected to be used for the quality control of turbine blades. The quality control and failure analysis are an important part of the manufacturing process. The ability to correctly identify vibrational modes and strains within turbine blades are facilitated by new generations of printed sensors. The novel designs give our corporate sponsor a technological edge. In particular being able to create strain gauges of any arbitrary geometry and location is an utility that is not curretly availble to the quality control teams.

The very nature of the substrates is of interest to this work as well. The printing process highly dependant on the surface interactions between the material being printed on. In the intended applications the base substrates are conductive. These substrates are usually prepared with a film of insulating ceramic material such as alumina. There are few such substrates available to research as most pieces are for production. Obtaining research materials is cost and time prohibative. The development of sol-gel processing alumina films is to support the thesis work herin to replace the insulating layers typically found on these blades.

1.0 Strain and Measurements

Strain (ε) is a measurement of a material`s deformation. It is measured in one dimension by the change in length of the material normalized by the original length of the material.

$$\varepsilon = \frac{dL}{L} \qquad \text{Equation 1}$$

The strain of the material is related to the forces experienced on a material during use. These forces are stresses as defined in where σ is stress and E is the Young's Modulus. Strain can be linearly correlated for elastic materials to the forces it experiences by the Young's modulus of the material as in Equation 2. Stress analysis is a key element of machine wear testing.

$$\sigma = E \cdot \varepsilon \qquad \text{Equation 2}$$

A typical strain gauge is presented below in Figure 3. The concept of a strain gauge is that the strain is transferred to parallel high aspect ratio traces. The traces deform in a predictable manner according to the Poisson's ratio for the material. Poisson's ratio governs the ratio of deformation in the perpendicular and parallel direction of applied strain. This predefined deformation changes the cross-sectional area of the trace in the sensor. The change in cross section affects the resistance (R) of the device. The magnitude in change in the resistance (δR) is correlated to the strain on the device by a ratio known as the gauge factor γ.

$$\frac{\delta R}{R} = \gamma \frac{\delta L}{L}$$

Equation 3

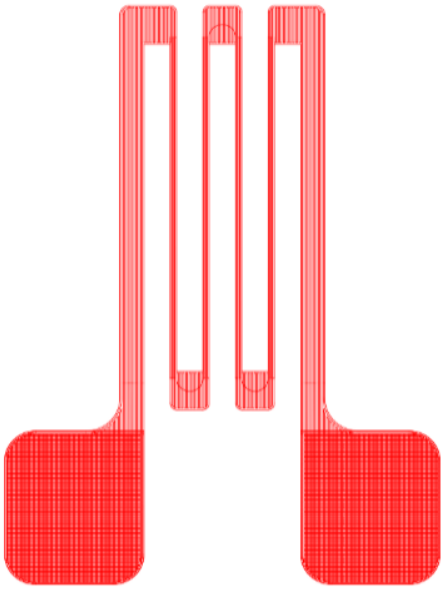

Figure 3 Typical Strain Gauge

Typical application of strain gauges is labor intensive. Strain gauges are created using thermal deposition techniques. Subsequently, they are adhered to the blade by manually placing each gauge in its required position. Each applied strain gauge can take a technician over an hour to place properly on a specific location. To properly characterize a strain field on a part multiple sensors may need to be placed as redundancy as well as to capture the full strain properties of the part [8]. The strain gauges with the lead attachments often disrupt the environment of in-situ tests in confined spaces. There exists a desire to print these gauges and traces on parts to help solve these problems.

1.0.1 High Temperature Applications

The objectives of my research study will be to create an ink that can form metal traces functioning as strain gauges in the temperature range of 1000-1100 ˚C. Well behaved materials are rare to find

in this temperature regime. This is because the resistance of a typical metal is very temperature dependent. Figure 4 shows this linear dependence on temperature. This eliminates many of the high temperature metals that are used in the structural components of the parts being tested. Without stability with regards to temperature the sensor will have too much noise to reliably generate signals. Metal alloys such as nickel chromium alloys (NiCr) are used as electrical components just below the targeted temperature of the project. NiCr's well-tempered behavior in the temperature regime can be attributed to the fact that the chromium alloying elements allow for a different resistance pathway than in typical metals. The resistivities of these NiCr alloys are orders of magnitude higher than regular nickel metals. The failure mode of the common NiCr starts to mechanically and chemically fail at the elevated temperatures required [9]. The target material as determined prior to the onset of this thesis was the palladium chromium alloy system (PdCr) developed by NASA in the early 90's. The material behaves very similar to the NiCr system but allows for a higher operating temperature due to the stability of the palladium over the nickel matrix. In Table 1 the properties of palladium chromium are listed. (P9)

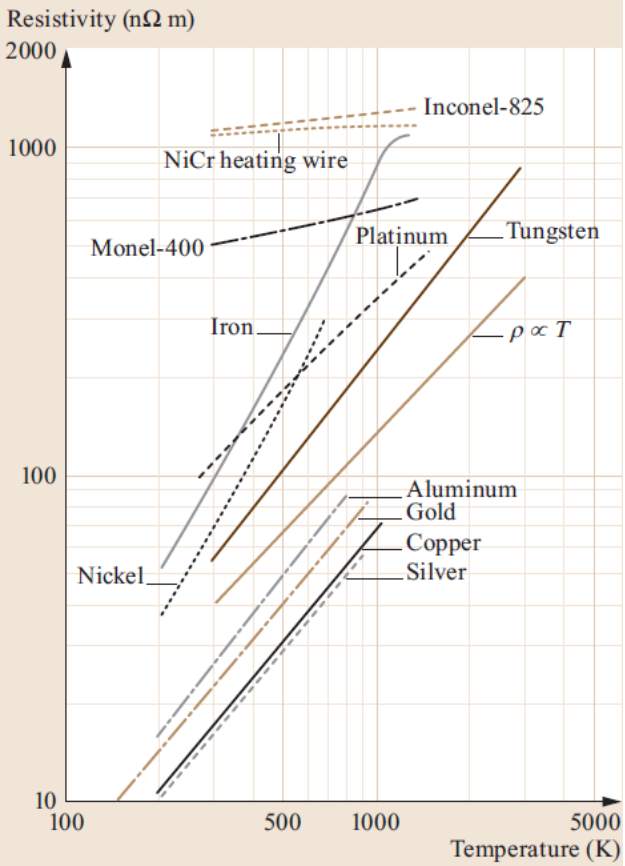

Figure 4 Metal Responses to Temperature [8]

The metal characterized by NASA was in the form of 115 um thick films [10]. Aerosol ink jet printed strain gauges by comparison typically have maximum minimum dimensions of 20 µm. This adds to the difficulty of the task as the metal operates in these high temperature regimes by providing a native oxide of chromium oxide that can be as deep as 15 µm. Such oxidation would result in a catastrophic failure of the strain gauge. Such challenges will be the focus of this work.

Table 1 NASA's static strain gauge targets [7]

Property	Value
Repeatability Difference in resistivity in heating at 10K/min and 250 K/min	2,700 and 1,900 (μΩ/Ω) at room temperature and 1250K
Oxidation Resistance Mass gained due to oxidation	+0.59 (mg/cm^2) (After 50h at 1250K) Typically ~2 μm oxide penetration (max 15 μm)
Resistivity	82 (μΩ cm) (R.T)
Temperature Coefficient of Resistivity	153 (μΩ/ (Ω K))
Elastic Range	740 / 332 (με at room temperature and 1250K)
Thermal Expansion Match to Substrate	13.8 (μm / (m K)) Super alloy: 15.5 ppm/K Al2O3: 7 ppm/K
Drift in strain over 3 h at 1250 K	50 ppm

1.1 Objectives

The objective for this work was to create an ink capable of producing a strain gauge to operate at temperatures meeting or exceeding 1250 K. An ink's components include the metal filler, solvent matrix, binder, and dispersant. The constraints on the ink are derived from the nebulation and jetting stages of the printing. The droplet size delivered is in the range of 1-10 um; as such the metal particle must be sub 100 nm for the droplet formation to be stable [11]. If a particle approached the size of the droplet it would significantly affect the surface tension of the droplet which is critical in the droplet formation stage.

1.2 Expected Design Challenges

The palladium chromium (PdCr) alloy has been employed by NASA as a strain gauge material at high temperatures for two reasons. Firstly, the PdCr alloy has non-temperature dependant resistivity behaviours. Secondly, the metal forms an oxide passivation layer on the alloy surface preventing further oxidation [10]. However, the alloying level of chromium is problematic as the element diffuses out of the alloy to form the passivation layer. The chromium oxide layer will continue to grow at high temperatures such that a film of >5 μm will form in 10 h at 900˚C [12].

Having the PdCr alloy in the form of a nanoparticle can present challenges. Oxide formation at the nanometer scale will introduce impurities in the bulk material and reduce the overall conductivity of the deposited material as is seen in copper systems [13]. The density of the formed material must be as close to the bulk as possible to avoid enhanced corrosion problems. The impurities introduced by the nanoparticles and their associated chemicals make it difficult to pack nanoparticles into a dense state.

1.3 Design Criteria

The design of these nanoparticles will be considered a success if they fulfil the following criteria:

1) That the nanoparticles after appropriate processing will make a metallic alloy with the properties of PdCr alloys of chromium content 13 wt %.
2) That the nanoparticles be suitable to produce an ink that is processable by aerosol ink jet printing.
3) That the nanoparticles be stable in the ink for a reasonable amount of time. Target of greater than three months.
4) The final dynamic strain gauge should have an apparent strain sensitivity less that of 100 $\mu\varepsilon\ ^{\circ}C^{-1}$. As well as the drift rate at use must be less than 500 $\mu\varepsilon\ h^{-1}$. [7].

1.4 Design Philosophy

To address these issues in the nanoparticle design, a core shell nanoparticle can be made with palladium being the shell around the chromium. This idea comes from the analogous copper silver core shell systems. In those systems copper is protected against oxidation in normal circumstances by a silver shell [14]. The flow of the nanoparticle synthesis to the bulk materials is as follows:

1) Chromium nanoparticles are prepared from lab experiments or from commercial sources.
2) Palladium encapsulates the chromium to form a shell around the nanoparticles that is resistant to oxidation under ambient conditions.
3) The ink is formed and processed into desired pattern in ambient conditions
4) A pre-sintering heating is performed to remove any organic capping agents in the pattern at temperatures lower than that where the formation of metal oxides become an issue.

5) An alumina layer will be deposited over the device to prevent oxidation. Sol-gel technology will be useful in this approach [15]–[17].
6) A final sintering and annealing will take place to complete the sol-gel ceramic and allow diffusion of the metal solution to reach equilibrium.

1.5 Thesis Structure

This thesis will cover a broad literature review in chapter two that will serve as a further background and informational section to understanding the challenges presented. Chapter three will concern itself with the formation of inks for strain gauges as well as production of test gauges. Chapter four looks to the sol-gel insulation research done to prepare proper substrates for the use of strain gauges at elevated temperatures. Finally, chapter five will conclude and summarize the thesis and its findings.

2 Literature Review

2.0 Palladium-Chromium Material Literature

The main body of work in printable conductive materials covers materials such as copper, silver, gold and graphene [5], [18]. These studies occur at moderate room temperatures. Conductive inks functioning as strain gauges working at 1250 K have not been previously investigated. The material selection for strain gauges at 1250 K is limited [19]. The select materials known to us come from NASA's 1986 investigations for use in conventional strain gauges. NASA established palladium chromium (PdCr) alloy systems as the standard material for strain gauges operating at 1250 K. It is off of this work that ink preparation has been established [10],[20].

2.0.1 Turbine Energy HOT Section Technology

2.0.1.1 Elevated Temperature Strain Gauges

Three traits are necessary for strain gauge operation at 1273 K. Firstly, the gauge should not undergo a temperature phase transformation. A phase change causes the crystal structure of the material to change. The changing crystal structure causes a nonlinear change in the electron scattering of the material that cannot be predicted or adjusted for. Secondly, any alloy used should exist as an ideal solid solution. Thirdly, the materials have to be chemically and thermally stable to reduce oxidation and mechanical wear during use [10]. These three traits provide stability of sensor operation.

Typical noble metals are not suitable for strain gauge operation at high temperatures. By example, palladium has a coefficient of thermal resistance (CTR) of 4 μΩ/Ω / ˚C which is too high for strain

gauges [21]. Silver alloying with palladium was tried as silver has a lower CTR. However the silver oxidizes causing drift in the electrical signal from the gauge.

The high temperature strain gauge has additional design challenges due to apparent strain on the sensor. The apparent strain is the error in the device measurement that directly interferes with the strain measurement.

$$\varepsilon_{measured} = \varepsilon_{real} + \varepsilon_{apparent}$$

Equation 4

For high temperature strain gauges the apparent strain is important because it is a strong function of temperature:

$$\frac{\delta \varepsilon_{apparent}}{\delta T} = \frac{1}{\gamma}\frac{\delta R}{\delta T} + \Delta CTE + \frac{\delta \varepsilon_{apparent}}{\delta t}$$

Equation 5

Where ΔCTE is the mismatch in thermal expansion between the strain gauge and the underling substrate. δt in Equation 5 is a time derivative known in strain sensors as thermal drift. The drift captures the chemical changes to the material that affect the strain reading.

The thermal coefficient of resistance and the thermal drift both pose challenges at elevated temperatures. The thermal coefficient of resistance is a normalized measure of how the resistance changes with temperature and is a function of the thermal mismatch with the substrate and the change in resistivity with temperature.

$$R = R_0\big(1 + CTR(T - T_0)\big)$$

Equation 6

Where R is the resistance of the conductor and R_0 is the resistance at temperature. The linear increase in metals comes directly from the vibrations of the lattice atoms [8].

Classically the lattice atom's kinetic energy can be modelled as:

$$KE_{Scatter} = \frac{1}{2} M a^2 \omega^2$$

Equation 7

where a and ω are the amplitude and frequency of the scattering atoms. Taking KE to be on the order of kT, a is proportional to $T^{1/2}$. With the electron scattering cross-sectional area S given as:

$$S = \pi a^2 \propto T$$

Equation 8

$$\mu_T \propto \tau_T \propto \frac{1}{S} \propto T^{-1}$$

Equation 9

Where μ_T, τ_T will be denoted as the thermal mobilities and mean free time of the electron in the conductor.

If the $\mu_T \propto T^{-1}$ then the $\rho \propto T$ as $\rho = \frac{1}{ne\mu_T}$ where n is the electron concentration and e is the elementary charge constant.

In a perfect crystal bulk conductor the resistance is:

$$R = \rho \frac{l}{A}$$

Equation 10

For the purposes of high temperature strain gauges however; the resistivity term is not purely dependent on thermal effects. According to Matthiessen's rule the resistivity can be broken into three components:

$$\rho = \rho_T + \rho_I + \rho_D$$

Equation 11

Where ρ_T is the thermal scattering described above, ρ_I is the scattering due to impurities in the metal and ρ_D is the scattering due to defects within the structure.

By understanding the nature of the coefficient of thermal resistance we can begin to engineer uses for such materials in strain gauges. NASA's best approach to minimizing the TCR of the materials they tested was to increase ρ_I to the point where ρ_T was not significant to the overall mechanism. As such, the palladium chromium alloy was first identified by NASA in a document published in 1986. The palladium chromium mixture succeeded in the material selection performed at the time because of the chromium alloying component provided both temperature insensitive impurity scattering centers and a self-protective oxide layer.

Thermal drift in the strain gauge material comes from the third term in Matthiessen's rule, ρ_D. Extreme temperature effects like creep oxidation and corrosion manifest as thermal drift. These effects cause defects. The defects in the material change over time and temperature as defects become more mobile and move or propagate due to the thermal energy. Thermal drift is the electrical sensor response to these irreversible changes. Typically strain gauges measurement capabilities and the mechanical integrity of the high temperature material will fail.

Figure 5 is the phase diagram for the palladium chromium alloy system. The phase diagram gives the expected crystal structure for a given composition and temperature. It is possible to determine the distributions of phases of the expected mixture of metals by looking at where they lay in the diagram. The binary solid solution is thermodynamically stable up to 13% chromium by weight. Any more chromium in the mixture and the alloy will form a Cr_2Pd_3 intermetallic phase to reduce the energy in the system. Coincidently NASA found that the 13% weight alloy was the optimal path forward with the alloy system. Slight reductions of chromium concentration due to loss to the protective oxide layer have minimal electrical impact. The alloy system works as an ideal solid solution at this concentration. At 17% alloying content, the alloy has drift rates of 837 ppm/h. Other metal additives to the solution lower the TCR and raise the drift rate to unacceptable levels [22].

The electrical resistivity of pure palladium is 10.56 μΩ cm [21]; whereas NASA found the PdCr13 to have a resistivity of 82 μΩ cm at room temperature. The increase in resistivity is due to the chromium impurities that help lower the overall effect of temperature on the material.

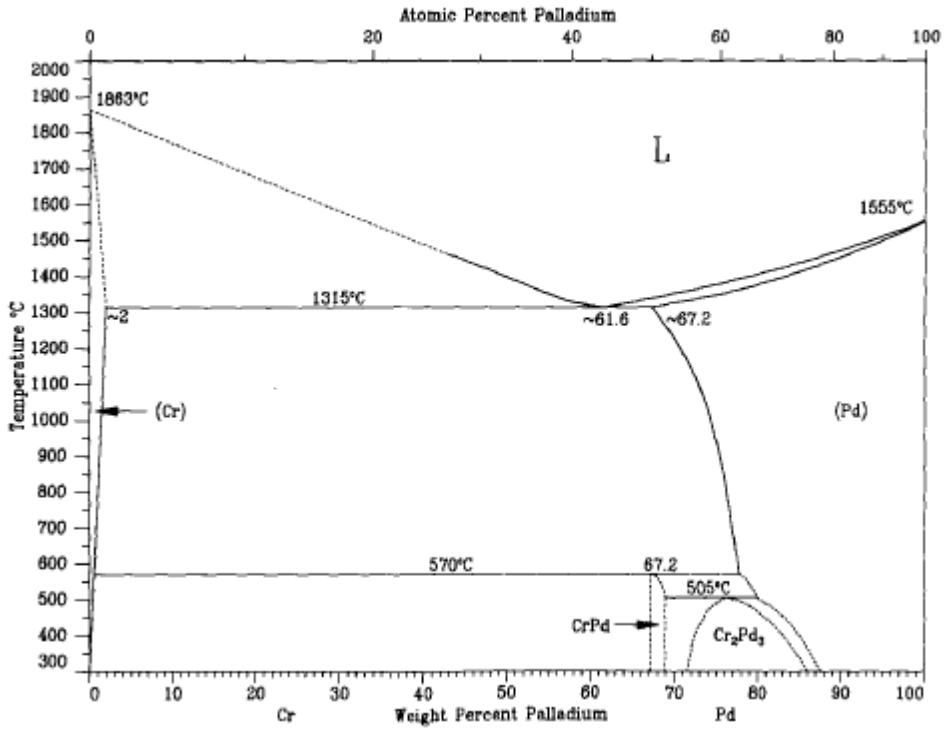

Figure 5 Phase Diagram for Palladium Chromium [23]

2.0.1.2 Development of High Temperature Static Strain Sensor

PdCr printed strain gauges behave like a thin film. Thin films have consequences on the performance of strain gauges. Notably the specific surface areas are greater. The corrosion properties of the gauge are more difficult to engineer than if the material existed as a bulk wire.

Difficulties occur when one tries to make smaller features of chromium oxides. The smaller features increase the effective surface area of the material. Figure 6 gives the amount of chromium needed in the alloy to form 0.59 mg/cm^2 of oxide on a spherical particle as is typical [22]. The material itself cannot provide reliable oxidation resistance when the feature size is below 100 μm.

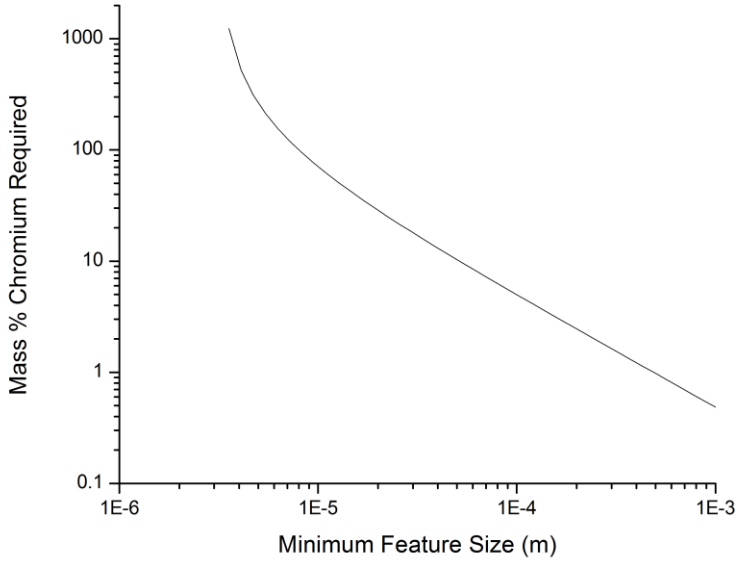

Figure 6 Amount of Chromium Depleted by Oxide layer

At high temperatures the elastic range of the PdCr13 alloy is reduced from 740 με to only 332 με [20]. The shortened elastic range means that the error in drift is larger compared to the signal obtainable from the strain gauge. Yet this is the best material known to us. PdCr13 has a drift rate of 50 με/h in bulk. Kenthal in comparison has a drift of 3480 με/h with an elastic range of 571 με at 1250K [22].

The failure mode of PdCr13 alloys closely mimic that of pure chromium. Firstly, the main failure is oxide layer detachment which occurs at 1223 K after one hour. Secondly, the oxide growth proceeds by the chromium ion diffusion through the oxide surface to react at the surface. Finally, starting at 1173 K formation of a Cr_2N phase was observed at the surface of the alloy. The nitride layer is a denser protective layer but it is typically kinetically formed as the oxide is thermodynamically preferable [24]. It is to be expected that for higher surface area features that these temperatures of failure occur at lower temperatures.

Metal alloys were the only type of materials investigated. Ceramics such as ZrN, TiN, and TiB_2 may be stable up to 1500˚C. They were avoided due to their toxicity and the instability of the nitrides in atmospheric environments [9], [25]. The PdCr13 system outlined is the most promising of all the alternatives.

2.1 Chemical Reduction

The chemical reduction technique allows for the creation of nanoparticles with control over the composition and size. The chemical reduction process creates free metal species which undergo three distinct phases, nucleation, growth and termination. The free metal species are created by a redox reaction between two chemical species. Typically, a reducer with a lower electronegative potential donates electrons to an oxidizer, which in this process is a metal salt. In the nucleation phase, the free species nucleate into the seed particles. In order to overcome the energy barrier of forming new surfaces and the decrease in entropy, high concentrations of free species must be present in a solution. The small particles exit nucleation at 1-5 nm in size. The second stage is termed growth. It occurs when the metal atoms add to the existing particles formed by nucleation. The third stage, termination, occurs as a stopping point for the growth. The termination is usually accomplished by either capping the particles by a passivation layer or the depletion of the growth species. The capping layer that terminates the particles is important because at these small sizes the effects of surface area tend to dominate. Oswald ripening is such a surface area effect. In Oswald ripening the species that are at the surface of the particle are in equilibrium with the surrounding solution. Consequently, the chances that a species leaves a small particle and deposits onto a larger one is amplified due to the increase in surface area. Oswald Ripening should be prevented to achieve the narrow size distributions that are desired for aerosol ink jet printing.

The degree of difficulty of making the intended nanoparticles through the chemical reduction technique is complicated by a couple aspects of the endeavor. The first is that the intended material exists as an alloy. The two components of the alloy make it a more difficult task to perform reduction simultaneously. Secondly chromium is much more reactive than palladium. Chromium dominates the engineering considerations for reduction as well as introducing significant corrosion possibilities.

2.1.1 Thermodynamics

As a first stage, the initial species formation reaction will be considered. For the salt of the metal to gain electrons from a chemical species the overall reaction must have a negative, Gibb's Free Energy,ΔG.

$$\Delta G = \Delta G° + R_g T ln Q_r \qquad \text{Equation 12}$$

Where:

- $\Delta G°$ is the free energy per mole of the reaction for unmixed chemicals at standard temperature, pressure, and concentrations
- R_g is the gas constant
- T is temperature in K
- Q_r is the reaction quotient which is the ratio of reactants and products currently in the reaction.

In an electrochemical reaction such as reduction of the metal salt Gibbs free energy can be defined in another way:

$$\Delta G = -nFE_{cell} \quad \text{Equation 13}$$

Where:

- n is the number of moles of electrons transferred in the reaction
- F is the Faraday constant (96585 C/mol)
- E_{cell} is the cell potential

The cell potential is measured in the voltage and is derived from the potential difference in chemical energy between two species transferring electrons. Cell potential may be tracked by using standard potentials measured at the standard conditions:

$$E = E° - \frac{RT}{nF} \ln Q_r \quad \text{Equation 14}$$

And at room temperature for a single electron transfer:

$$E = E° - 0.0257 \ln Q_r \quad \text{Equation 15}$$

Therefore, in reference to Equation 13 the total energy change can only be negative if the electrochemical cell potential is positive which is required for spontaneous reactions.

The standard cell potential $E°$ above can be defined as:

$$E° = E°_{reduction} - E°_{oxidation} \quad \text{Equation 16}$$

As such the reaction can only proceed if the reduction potential of the reducer is less than that of the metal salt being oxidized. This presents the first problem in making the palladium chromium alloy particles. Unlike more common noble metals that are reduced to form nanoparticles,

chromium has a much lower electrochemical potential. Using Table 2 and Table 3 to compare potentials with reducing agents, we find chromium is much lower in potential than the common reducing agents.

Table 2 Metal Salt Potentials

Species	Electrochemical Potential (V)	Reference
Pd^{2+}	0.951	[26]
Cr^{3+}	-0.744	[26]
Cr^{2+}	-0.913	[26]
$Cr(OH)_3$	-1.48	[26]
CrO_2^-	-1.2	[26]
Au^+	1.7	[26]
Ag^+	0.8	[26]
Cu^{2+}	0.34	[26]
H_2O	-0.83	[26]

Table 3 Reducing Chemical Potentials

Species	Electrochemical Potential (V)	Reference

Sodium Citrate	-0.180	[27]
Hydrazine	-0.33	[28]
Sodium Borohydride	-0.481	[26]
N-Butyl Lithium	[-1.0, -2.0]	[29], [30]

The lower potential means that the traditional chemical reducing agents must have an extremely high Q_c or concentration for the reaction to be favorable in ideal conditions. Even if these reactions are favourable it doesn't indicate that they will be kinetically favourable. Additionally, the electrochemical potential of chromium is very near that of the electrolysis potential for water indicating that the reactions involved with making these particles may cause side reactions with aqueous solvents.

2.0 Core-Shell Nanoparticles

The analogous system to PdCr13 in current printed electronic work is silver copper alloys. Much of the pioneering printed electronic work has been performed with silver [31]–[34]. Work to make these systems cheaper involve the substitution of silver with copper. However, copper has a lower electrochemical potential than silver. Silver has a potential of 0.8 V and copper 0.3 V [35]. This slight decrease has the ramification that the copper is much more easily oxidized in ambient and

humid conditions. The solution to these problems has been to encapsulate the copper nanoparticles with a silver shell, effectively surface modifying the copper with the less reactive silver [36], [37].

Core shell particles may be produced by different techniques such as galvanic displacement or thermal decomposition and reduction [13]. Thermal deposition is a process where neutral charged complexes are thermally degraded to form the nucleating metal species. The metal species then may migrate to the surface of preformed seed particles to form a shell. In galvanic replacement reactions, salts of a higher chemical potential are introduced to the metal seed particles. Due to the potential difference between the two species the replacing species reduce on the surface of the seed while oxiditively etching the seed particle.

Making a shell of noble metal on a chromium particle has been reported previously [38]. When chromium salts are reduced with sodium borohydride and encapsulated with platinum, most of the chromium in the particle is oxidized. The particles produced were a mixture of nanoparticles that had a bimodal particle size distribution and different elemental compositions as determined by STEM. The smaller particles were pure platinum particles that nucleated apart from the chromium nanoparticles. The larger particles were found to have a platinum chromium core with a Pt Cr_2O_3 shell. While the presence of platinum in the chromium core was explained by Cabrera—Mott theory [38], the oxidized chromium at the surface was found to exist in a 4:1 ratio with the chromium metal.

Chromium nanoparticles have also been attempted to be produced by borohydride reduction [39]. This was achieved by reducing the salts with superhydrides in the presence of trialkylphosphine oxides. The main observation is that for the chromium nanoparticles they observed XRD

reflections between 40˚ and 50˚and again between 55˚ and 70˚, which give the 200, 210, 211, 220, and 310 crystal planes for the BCC chromium particles.

Due to the inherent reactivity of the chromium in the alloy, some form of mitigation must be designed into the produced nanoparticles. This work focuses on the concept of creating a shell of less reactive material around the chromium particle to mitigate the reactivity. The approach clearly splits the ink formation into two separate stages. In the first stage chromium nanoparticles are prepared in an inert environment and in the second a palladium coating is applied to the surface. In context of the Druid-Mathieson model of oxide growth the coating of palladium would serve as a diffusion barrier for the charged chromium species migrating to the surface.

There are a few difficulties with the approach as described. There exist the assumptions that the chromium nanoparticles can be prepared without an insulating capping layer attached or that the capping layer can be permeable to the palladium growth species. The palladium is not guaranteed to grow conformally on the chromium seed, or even in excess concentrations the palladium growth species will self-nucleate forming pure palladium particles.

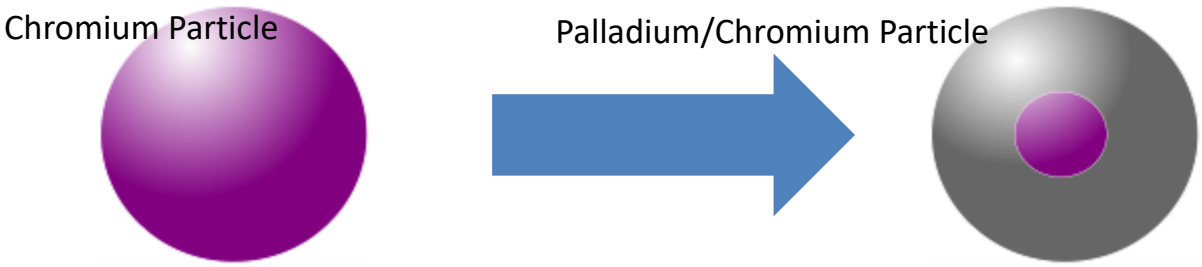

Figure 7 Core Shell Nanoparticles

2.0.1 Capping Agents

Aggregation occurs between the metal particles in the ink causing the solids content to decrease over time. To avoid aggregation, nanoparticles have another shell encapsulating them. This shell is the capping layer. The capping layer for metallic inks must fulfil the following basic requirements:

i. To prevent the aggregation of the particles
ii. To suspend the metal particles in sufficient weight concentrations
iii. To decompose cleanly leaving little carbon residue in the part
iv. Prevent Oswald ripening of the particles
v. Have proper surface tension modifications of the carrier solvent.

To these ends the capping agent polyvinylpyrrolidone (PVP) has been selected due to the abundance of its use in literature for these purposes [40]–[44]. The chemical structure of PVP is given in Figure 8 below. PVP is a polar molecule that is easily soluble in other polar solvents. The

lone pair of electrons on the nitrogen and the high electron density of the carbonyl coordinate the polymer on the surface of metal nanoparticles [42].

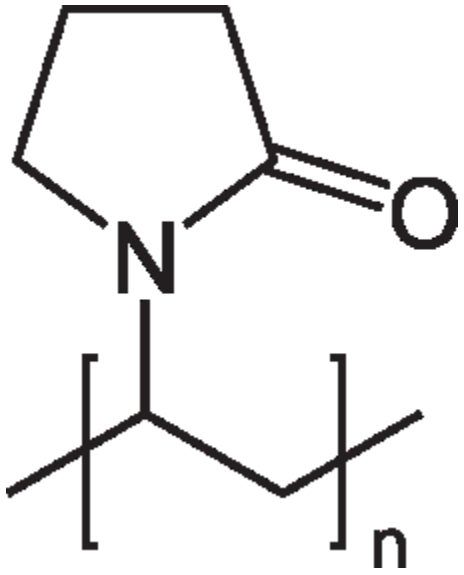

Figure 8 Chemical Structure of Polyvinylpyrrolidone

PVP is widely used in all aspects of nanoparticle synthesis [40]. PVP can act as a diffusive barrier, shape control agent, dispersant and reducing agent. PVP is known to degrade in inert environments starting just below 400˚C and it absorbs preferentially on palladium surfaces to control the particle size produced. The palladium nanoparticles will catalytically decompose the PVP at lower temperatures especially in reducing environments used to sinter the nanoparticles [45]. PVP does not combust cleanly leaving carbon soot a poison in the sintering processes.

2.1 Reaction Conditions

2.1.1 Palladium Salts

For all synthesises here presented plan palladium acetate will be used as the source of the palladium ions for reduction. The nitrate salt is preferable to the halide salts because it has been observed that the halide salts aid in oxidative etching of nanoparticles [46]. As well the organic salt will slow down the reduction process facilitating the formation of core-shell nanoparticles [47]. The phase diagram for the reduction of palladium salt is given in Figure 9 below. The phase diagram shows the most thermodynamically favourable state for the metal salt to be in given an electric potential in a solution at a certain pH. It can be observed that not much potential is needed for this reduction and that the formation of the palladium metal is favoured in more acidic conditions.

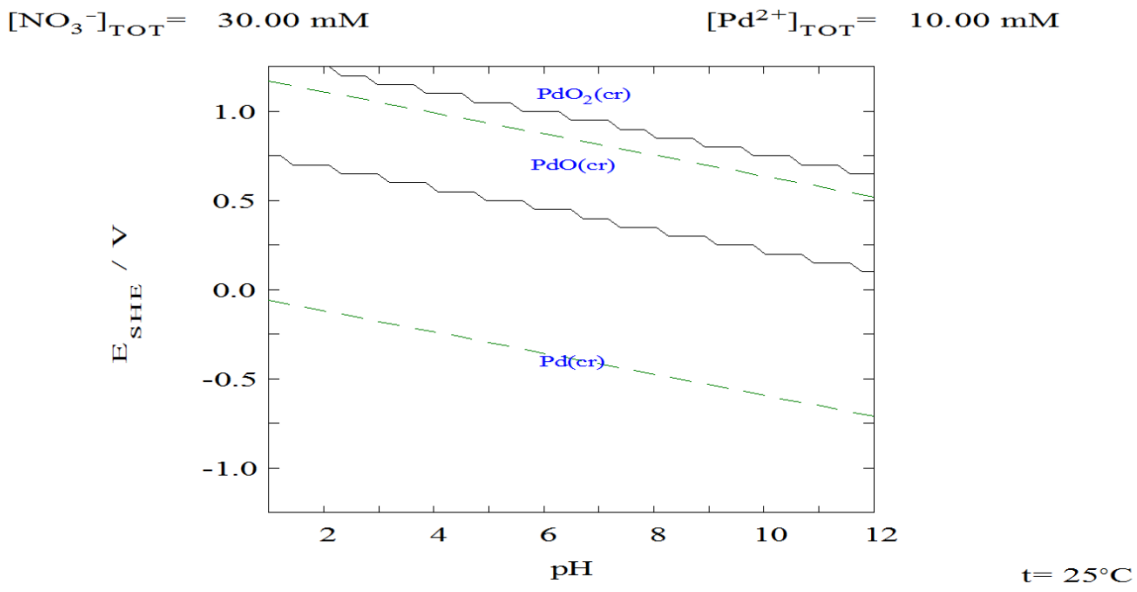

Figure 9 Palladium Equilibrium Diagram [48]

2.1.2 Chromium Salts

For the reaction attempts with chromium, chromium acetate will be used as the chromium salt to provide the chromium for the reduction. This is a deviation from the chromium nitrate that we have previously used. The reason for this is twofold. Firstly, it prevents the formation of nitric acid that may form in the solution. Nitric acid is an oxidizing acid that will react violently with the strong reducers needed to be used in the reduction of the chromium salts. Secondly the acetate may thermally decompose in the reaction destabilizing the salts. This has been shown to be an effective reductive process for other hard to reduce metals such as nickel and lead [49]. The difficulty of reducing chromium may be elucidated in the Pourbiox diagram given in Figure 10. A Pourbaix diagram is a diagram of the thermodynamic equilibrium states of a metal-electrolyte system.

Different ionized species will exist at different cell potentials and pH. Strong acidic and reducing behaviors are needed to enable chromium metal reduction and avoid chromium oxide formation.

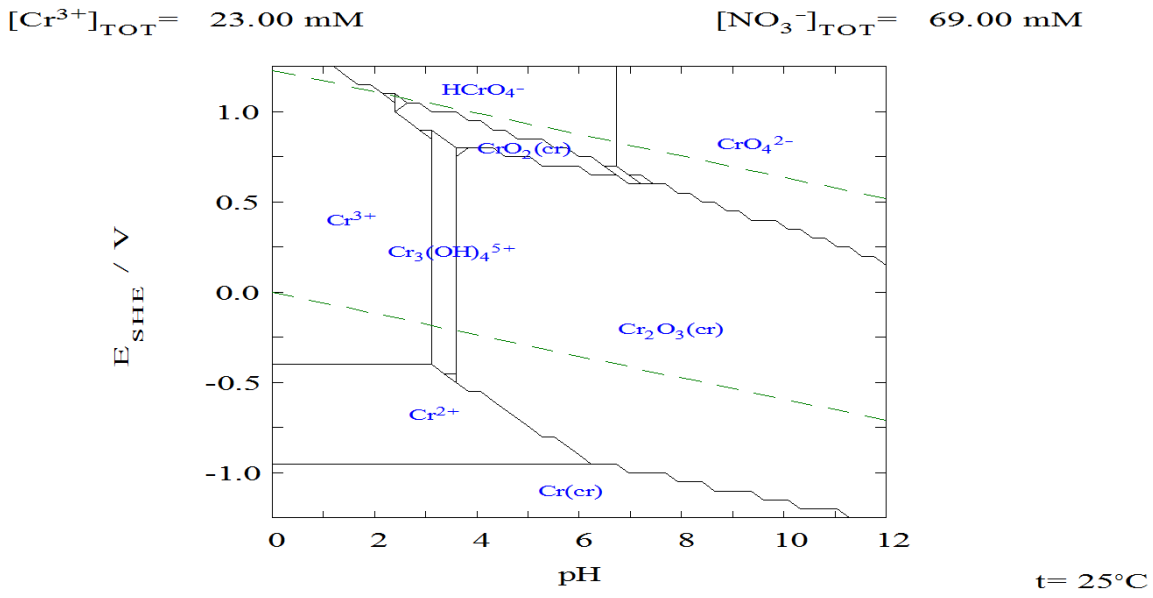

Figure 10 Chromium Equilibrium Diagram [48]

2.1.3 pH

In a non-reducing environment, the pH of the metal salt storage solutions must be considered to prevent oxidation. Figure 11 gives the logarithmic concentrations of aqueous species in the palladium nitrate system for various pH levels. The initial concentration of ions is typical for a chemical reduction.

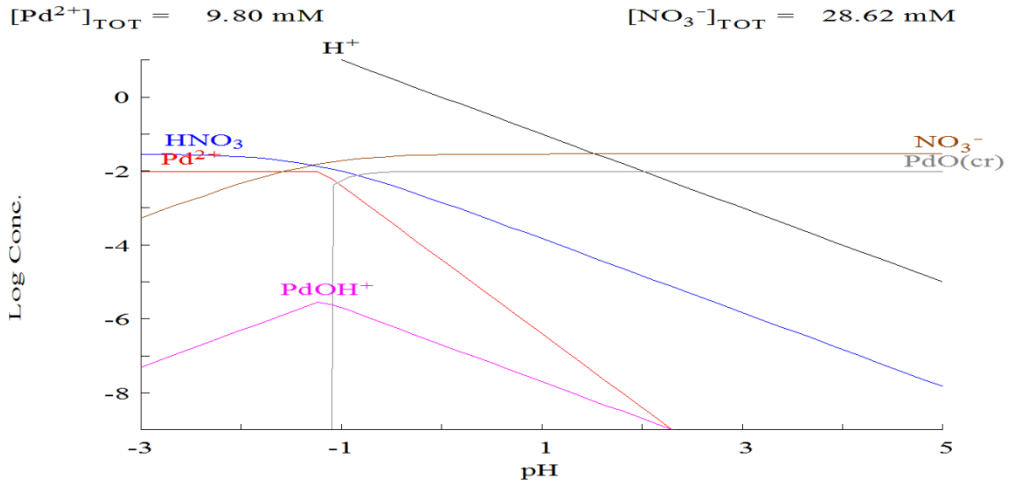

Figure 11 Palladium Species in solution [48]

An extremely acidic solution is necessary to stabilize the palladium ions in solution. The acidity remained a crucial component throughout all tried chemical reduction pathways. It's also important to avoid the hydroxide formation of the salt before the reaction as well. It is known that palladium hydroxide complexes readily form in water conditions which tend to create local high concentration areas of palladium. These local clusters produce high concentration of palladium free species when reduced often nucleating and disrupting the nanoparticle formation process [43], [50].

2.1.4 Solvent Choice

The solvent choice is of import as there are concerns with the oxidation of chromium nanoparticles. The solvent system worked with was a dual mixture of ethylene glycol and acetic acid; partly because these solvents could be purchased anhydrous and because they suited the reaction

conditions. The acetic acid was a solvent that could suspend the chromium acetate and it was found that the addition of acetic acid aided with the stability of the particles during the reaction. The acetic acid also had the benefit of not introducing new species to the reaction as the acetate ion was already present from the chromium acetate. The ethylene glycol served as both a solvent and a reducing agent for the reaction.

The mechanism of reduction by the ethylene glycol is not plain. The key reaction here is the ethylene glycol converting to its aldehyde according to [51]:

$$HOCH_2CH_2OH \rightarrow CH_3CHO + H_2O$$

And the aldehyde can act as a reducing agent to convert the metal salt to a free metal atom.

$$Pd^{2+} + 2CH_3CHO \rightarrow CH_3COCOCH_3 + Pd^0 + 2H^+$$

The basis for the chemical reduction techniques is derived from high temperature polyol synthesis hybrid techniques. Ethylene glycol has been shown to be a good solvent for these types of metal salts and reducing agents [52][53][44]. In addition to this ethylene glycol can be refluxed at 190˚C allowing us to thermally decompose the chromium acetate.

Acetic acid in the reaction holds a complex role. Acetic acid is a common solvent for nanoparticles. Originally, it was added to the ethylene glycol to adjust the solubility of the solvent towards solvating the chromium nanoparticles. Subsequently we observe that the acetic acid plays additional roles in the reaction. The first side effect is that it made the reaction solution acidic. The acidity slows down reaction as at pH 2-3 the concentration of H^+ is increased. The second is that the acetic acid reacts with the ethylene glycol to form an ester according to [54]:

$$HOCH_2CH_2OH + HOCOCH_3 \rightarrow HOCH_2CH_2OCOCH_3 + H_2O$$

The resultant molecule is ethylene glycol monoacetate. The ester group acts as a more strongly electron withdrawing group. The ethylene glycol monoacetate is more readily converted to the aldehyde due to the withdrawing effect, as well the monoacetate solvates the nanoparticles better.

The solvents also must be able to readily dissolve the salts of the reaction. Palladium nitrate as a source of the palladium salt is the choice in the synthesis as mentioned above. Palladium nitrate dissolves easily in polar or aqueous substances making it a facile salt to work with. Unfortunately palladium nitrate is also susceptible to forming hydrates that effectively pre-nucleate the palladium into clusters [55]. To avoid this, the solvent dimethylformamide (DMF) is used to solvate the nitrate salt, hence avoiding the hydrates. The DMF does not actively participate in the reaction and is miscible with the above solvent selection.

Where there are solvents usually there exists some form of water as well. Often water contains excess dissolved impurities including oxygen gas and the reaction was often carried out in the dry inert glove box. This ruled out water as a solvent for the reaction.

2.1.5 Core Shell Formation and Reaction Rate

Given a source of chromium nanoparticles the formation of a protective palladium shell is mainly a reaction rate problem given the ease of reduction. If the reaction proceeds too quickly the free palladium concentration becomes too high and the species start forming their own particles rather than depositing on the seeds of chromium. If the reaction proceeds too slowly the procedure becomes difficult to monitor and aggregation issues start appearing.

2.1.5.1 Controlled Diffusion

2.1.6 Chelating Agents

Other chemicals may be added to the solution to control the free palladium species as well. These are typically called stabilizing agents or chelating agents. These chemicals work by temporarily binding the palladium species to prevent their participation in the nanoparticle formation process. For our reaction process the choice chelating agent to work with is ethylenediaminetetraacetic acid (EDTA). EDTA uses the carboxylic acid groups to bind to the free ions in solution diminishing their reactivity.

EDTA is used as the secondary capping agent for the nanoparticles. The original inclusion of this compound was to lower the reduction potential of the added palladium salts. This would slow the reduction rate as necessary for the reaction to proceed at an appropriate rate. We have subsequently found that this compound plays a critical role in the stabilization procedure of the particles. Without the EDTA being in sufficient quantities the particles that settle out in the reaction cannot be suspended in the ink.

2.2 Aerosol ink Jet Literature

AJP as an emerging technology offers new capabilities when compared to its predecessor ink jet printing. The aerosol ink jet printer fundamentally deposits differently than an inkjet printer. Figure 12 illustrates the differences. The inkjet printer forms lines by continuous droplets that merge

together. In the aerosol process the printer lays down a continuous line of material.

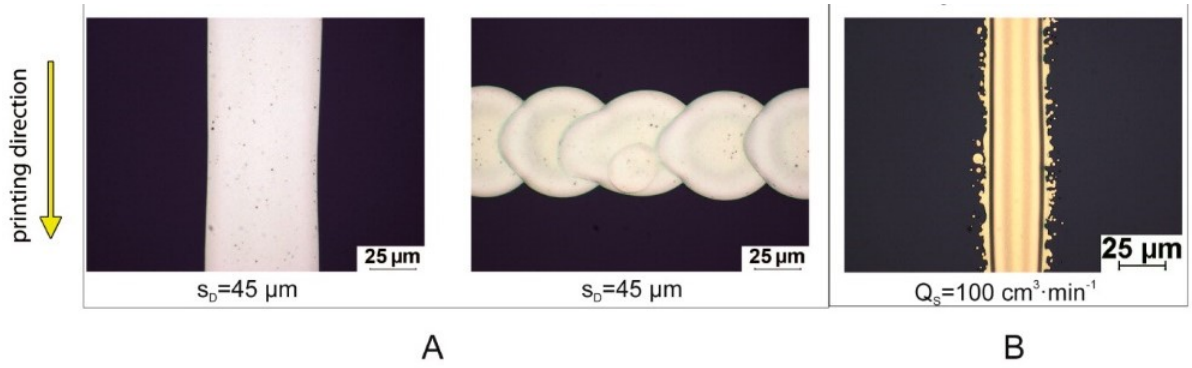

Figure 12 A: Line Printed by Inkjet Printing; B: Aerosol Ink Jet Printing [2]

The first step in the process is to make a liquid into micrometer droplets in a process called atomization or nebulization. To nebulize inks a vibrating disk is placed at the bottom of a liquid bath. The liquid when vibrated at a specific frequency forms a standing wave at the surface of the liquid or ink in the printer. This frequency is set to the ~2.5 MHz range for this particular printer. At this frequency cavitation occurs in the liquid. The cavitation produces shock waves which cause a standing wave on the surface of the liquid. The standing wave is in resonance and jets out small particles from the tip as the tip of the standing wave is not stable. The diameter of the droplet can be given by the equation [56]:

$$d_{droplet} = 2\pi c_1 \left(\frac{\sigma_l}{\rho_d}\right)^{\frac{1}{3}} \left(\frac{2}{\omega}\right)^{\frac{2}{3}}$$

Equation 17

And the power to aerosolize is given by:

$$P = \frac{m\eta}{\rho_d}\omega^2$$

Equation 18

where

- c_1 is an experimental factor equaling 0.35 ± 0.03
- σ_l is the surface tension of the ink
- ρ is the density of the fluid
- ω is the frequency of the driving water
- m is the mass of the wave
- η is the viscosity of the fluid

It is clear then that the size dependence of the aerosol and its ability to be aerosolized is dependent on the ink's fluid properties. It should also be mentioned here that all these properties are highly dependent on temperature and each of these effects can be seen in Figure 13 below.

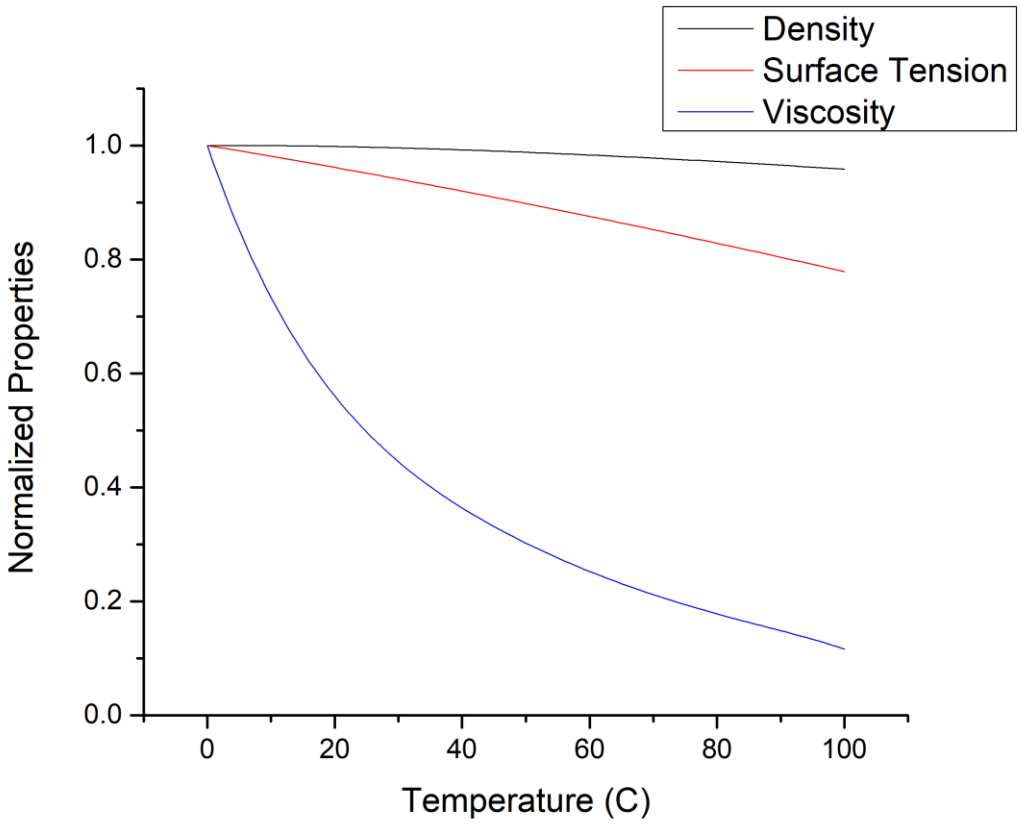

Figure 13 Temperature dependence of water fluid properties

The ink must consider these factors in order for processing to be easier. As the machine is limited to water frequencies, the chemical solvents for the ink will match those of water as closely as possible. However, it should be noted that water will be avoided due to the inherent oxidation problems associated with its use.

AJP uses gas streams to deliver the aerosol to the substrate.There are essentially two fluid flows in the aerosol ink jet printer, one gas flows through a reservoir of aerosol and the other gas flows encompasses that flow as a sheath [57]. The encompassing gas is known as the sheath gas while the reservoir gas is known as the atomizer gas. The sheath gas makes the atomizer gas follow a smaller flow profile by being at a higher pressure than the atomizer gas flow. Since the tubes that

the gasses are flowing through are sufficiently small the Reynolds number of the flow can be assumed to be below Re = 2320. The typical maximum Reynolds number is 800 [57]. This results in what is called laminar flow. In laminar flow the gasses flow straight and do not mix. This allows for the squeezing of the inner flow that carries the ink. The flow through the nozzle can be described like a capillary and as such is covered by the law of Hagen and Poiseuille. The flow shape is then described by the following equation:

$$U(r) = \frac{2(V_{atomizer} + V_{sheath})}{\pi R_{tip}^2}(1 - \frac{r^2}{R^2})$$

Equation 19

The diameter of the aerosol carrying flow can be obtained by performing the integral of the flow shape equation as the diameter of the aerosol is in the integration limits.

$$V_{aerosol} = \int_0^{2\pi} \int_0^{\frac{d_{aerosol}}{2}} U(r) dr d\phi$$

Equation 20

Solving Equation 20 leads to the following result:

$$d_{aerosol} = 2R\sqrt{1 - \sqrt{\frac{\chi}{\chi + 1}}}$$

Equation 21

Where χ is the ratio of the gas flow rates defined as $\chi = \frac{V_{sheath}}{V_{aerosol}}$ the velocity of the gasses is typically measured in ccm.

In printing systems there are two key mass transport stages. The first stage describes the formation and focusing of aerosol. The second is the transfer of the droplets from the gas stream to the substrate. Impact for the aerosol jet system depends on if the aerosolized droplets continue to travel

towards the substrate of printing when the airflow is disrupted by the impact of the air on the surface. The Stokes number controls this second stage. The Stokes number can be defined below:

$$Stokes = \frac{\rho_d C_c d_d^2 U}{9\eta^2 R}$$

Equation 22

Where:

- ρ_d is the density of the droplet
- C_c is the Cunningham correction factor which corrects for the assumption of the no slip condition that exists between the particle and the air around it.
- d_d is the droplet diameter
- U is the velocity of the droplet
- η is the dynamic viscosity of the air
- R_{tip} is the radius of the tip opening

If the Stokes number is much greater than one then the momentum of the droplet carries it through the deflecting air of the stream onto the substrate, else the small particle will be carried away from the printed pattern and appear as satellite droplets or escape the system entirely.

An understanding of how the printer operates is crucial in our efforts to design an ink for the machine to make high temperature strain gauges. The goal of outlining the above equations is to further the understanding of the underlying principles in the printing process.

The specific aerosol ink jet printer that will be used is called the Optomec AJ300 [58]. The specific machine promises flexibility, lower costs, and decreased prototyping time. The technology also

promises to be a large component in the green movement as additive manufacturing cuts down on the waste and caustic materials used in conventional manufacturing.

Ingredient	Function	Examples	Typical Amount (wt%)
Conductive Filler	Precursors or components of conductive material	Silver, Copper, Palladium, Metal Nitrates	10-60%
Dispersing medium	Continuous phase carrying the other components	Water, Ethanol, Toluene,	30-70%
Dispersant	Prevents aggregation	Polyvinylpyrrolidone (PVP), Polyvinyl-alcohols	2-10
Binder	Improve cohesion and adhesion of the ink	PVP, Resin, Glass Frit, Metal nanoparticles, Aluminum Based agents	3-10

2.3 Ink Formulation

Prior ink formulation work concerns itself mostly with inkjet printing. There is little precedent outside of patents on how to form ideal materials and inks for the aerosol inkjet printing process.

This section outlines with aid of previous literature on inkjet printing on how to properly formulate a conductive ink for uses of printing.

Ink components may be summarized as below:

Table 4 Components of Conductive Inks Adapted From [59]

There are a few special considerations for each of the above components in the ink, with each having its own selection criteria. The conductive material is usually straight forward as spherical nanoparticles with specific size distributions are required, if possible differently sized narrow distributions should be mixed for the best packing factors [60]. For the solvent there are additional factors to be considered, for the high temperature inks most importantly is the consideration of the oxidizability of the solvents as ketones have been known to be incompatible with copper and nickel particles. When ketones are used with these inks they chemically react to form their oxide. A second consideration is to avoid the effect termed “coffee ringing”. This is where upon drying the conductive particles tend to migrate to the substrate, droplet, air interface. This occurs do to the fact that the liquid at this interface evaporates more quickly than the rest of the liquid. The difference in evaporation rate causes a flow that moves the particles towards this edge. This can be offset by creating a counter flow within the droplet, this is termed Marangoni flow, by a concentration gradient. Park and Moon found that this can be accomplished by mixing two fluids with one with a low boiling point and low surface tension and the other with a high boiling point and low surface tension provides this type of counteracting flow [61]. The considerations for the dispersant keeping the nanoparticles apart is even more complex. In the most basic form any

chemical used must strongly stick to the surface of the particle yet another part of the molecule must remain bulky enough to keep enough distance between each particle by acting like a wrapping layer around each particle. On top of these requirements the dispersant must be compatible with the solvents identified. The dispersant operates on steric properties. The steric properties are controlled by the molecule's hydrodynamic radius. The measure of bulkiness used is the molecular weight of each polymer molecule used. The steric force must overcome the van der Waals force as defined:

$$U_{vdw} = -\frac{H_{p,m}}{6}\left[\frac{d_p^2}{2D\left(2d_p + D\right)} + \frac{d_p^2}{2\left(2d_p + D\right)^2} + \ln\left(\frac{D\left(2d_p + D\right)}{\left(d_p + D\right)^2}\right)\right] \quad \text{Equation 23}$$

Where:

- d_p is the particle diameter
- D is the distance between particles
- $H_{p,m}$ is the Hamaker constant of the particles in the medium

For the particles to be stable the thermal energy provided must be greater than the potential of the van der Waals force. This occurs at the inequality:

$$U_{T,min} = U_{vdw} \geq -3/2k_bT \quad \text{Equation 24}$$

Where k_b is Boltzmann's constant of 1.38 J/K and T is temperature.

For illustrative purposes a 100 nm gold particle with $H_{p,w} = 159.7\ zJ$ for two gold particles in water the equilibrium is found at approximately 30 nm.

Continuing with the illustration for capping agents on gold particles there is a useful equation predicting the length or hydrodynamic diameter of the capping agent in a medium as a first approximation.

$$l \approx 0.06(Mw)^{0.5}$$

Equation 25

In our example to obtain the 15 nm length required for 30 nm separation the molecular weight of the particle should be in the above the molecular weight of 57 kg/mol. It should be noted that the molecular weight has an upper limit of 300 kg/mol to prevent bridging of the chains which could entangle and join. Bridging occurs when the chains of the capping agent entangle together where the van Der Waal forces overcome the steric hinderance of the capping agents. The trade-off of a longer chain is that the longer the chain the harder it is to create dense connected particles when the nanoparticles are sintered together.

Now the most common dispersant for the use in conductive inks has been polyvinylpyrrolidone PVP as described previously. PVP binds strongly to the surface of palladium and yet a weaker bind to the hydride of palladium [62]. This property is ideal in the sintering process when considering the removal process.

Commercial aerosol ink jet inks outline key parameters for their operation. If different nebulizers such as pneumatic are used the viscosity should be in the 20-5000 cP at 10 sec^{-1} [63]. If the ultrasonic atmomizer is employed in contrast the viscosity should be below 5 cP and have a surface tension of ~ 60 dynes/cm [60], [64], [65].

2.4 Sol-gels

The sol-gel route to making ceramics is a chemical-based route that starts with metal organic precursors and polymerizes the monomers into ceramic particles and films. The sol-gels can be deposited by typical coating techniques such as dip, spray or spin coating. The process is illustrated in Figure 14 below.

Alumina sol-gel films have found uses in aircraft aluminum corrosion prevention as a replacement for chromium, optical properties, and dielectrics [15],[66], [67],. For dielectrics the film must be dense enough to block charge carriers from moving through the film [15], [17].

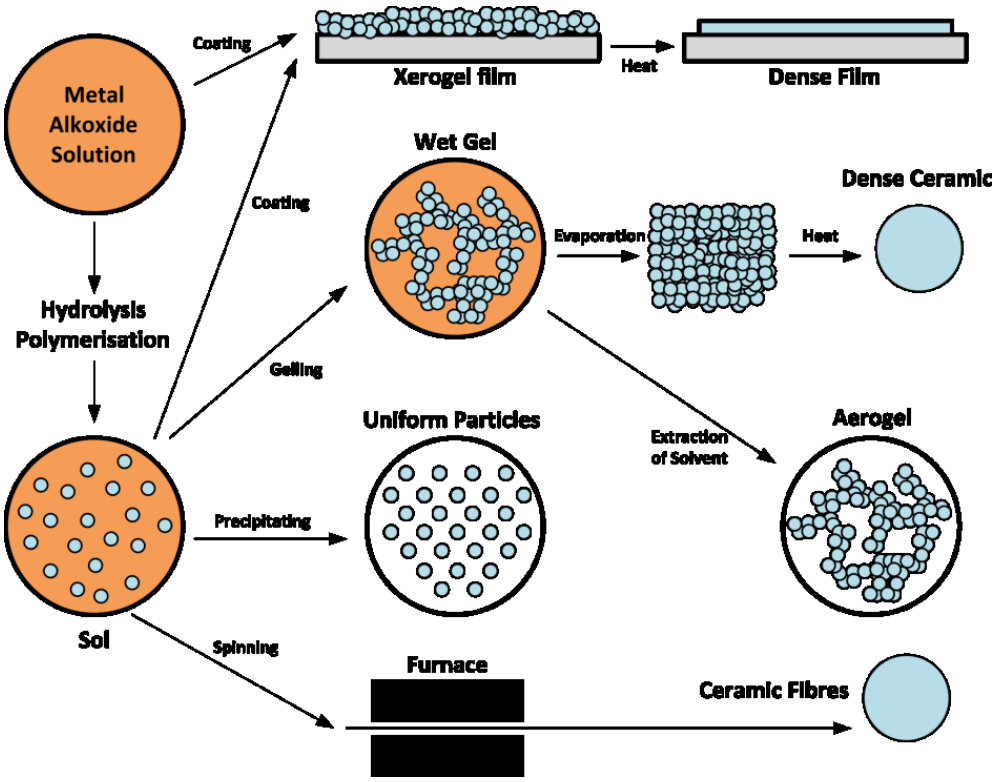

Figure 14 Sol Gel Process Creative Commons Claudionico 2013

2.4.1 Sol Gel Chemical Process Chemistry

The basis of sol-gel technology is the metal alkoxide precursor. Historically the most common precursors have been silicon based such as tetramethylorthosiloxane or tetraethylorthosiloxane as seen in Figure 15 and Figure 16 below.

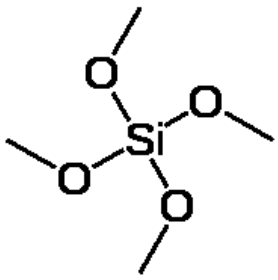

Figure 15 TMOS

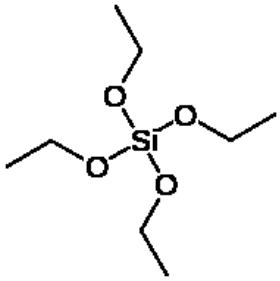

Figure 16 TEOS

What typically happens is that water will attack one of the side chains and leave a hydroxide group in its place. These hydroxide groups will react with other precursors to form metal oxide bonds. In this manner one can create metal oxide solids from the bottom up. By controlling the rates of these reactions different geometries ranging from nanoparticles to thin films can be formed. The main innovations in the late 20th century had to do with controlling this rate of reaction.

The main catalysts are acids and bases with both acting in different manners. Acids typically react in a SN2 type reaction with water displacing a protonated side group. With the base catalysed reaction the hydroxide ion will attack the metal center displacing a side group. The respective actions are provided below [68]:

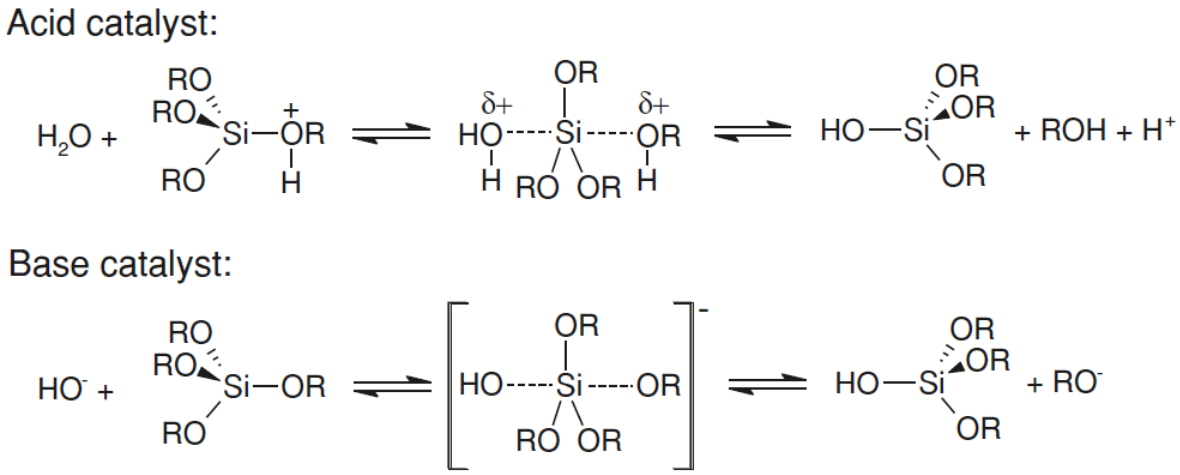

Figure 17 Catalytic Reactions in the Sol-Gel Process [68]

These types of reactions can generally be controlled by controlling the R groups in the metal alkoxide as well as adding additives to the solution. Also by altering the R group we can attach the precursor to metal substrates with ease [16].

Sol-gel formulations have been used as precursors for forming ceramics since 1970 [69]. The early inventions concerned themselves with producing porous ceramic powders for substrates in catalysis and the like [70], [71].

Sol-gels suffer from film cracking. These cracks are derived from residual stresses in the film formation process. There exists a critical thickness at which the film's cohesive forces are exceeded by the stresses in the film. This is given by Equation 26 below [72].

$$h_c = \frac{EG_f}{C\pi\sigma^2} \qquad \text{Equation 26}$$

E and G_f are the material's inherent properties, the elastic modulus and strain energy release rate respectively. C is a function that differentiates between the elastic properties of the film and substrate and σ is the residual stress in the film. Less crack prone films have higher h_c. To minimize the cracking problem the strain energy release rate will be increased as well as decreasing residual stresses in the film.

The sol gel process is a relatively facile process for creating ceramics with pores and voids so they are not fully solid especially in films. The problem with forming dense continuous films is due to the shrinkage incurred during the drying and curing stages in the sol-gel process [73]. Very recently research has turned to address the problem of forming crack free films in silicates [15], [17], [74]–[79]. These papers have elucidated the importance of the solution surface tension and vapour pressure in the film formation process. By slowing down the drying process the materials relax into a denser state for curing, however, most additives used to slow down this process decrease the solids content of the final cured ceramic increasing the porosity. The field of research has turned to increasing the sintered dry product by adding solid ceramic particles back into the sol-gel to create sol-gel hybrids. These hybrids have additional constrains in material compatibility as the particles must remain suspended in the sol gel solution.

The original plan by the GE Aviation team was to use an alcohol and metal alkoxide solution to formulate a sol gel coating [70]. The component ordered were aluminum sec-but-oxide and ethyl acetylacetone which according to the recipe would form a sol solution when added to isopropanol.

An improvement to the method proposed was to focus on making crack free films by preforming and partially hydrolyzing the sol gel into ceramic nanoparticles before casting the film [80]. In these schemes, the aluminum sec-butoxide is directly added to aqueous solutions to hydrolyze the

monomer. The hydrolysis is controlled by adding an equimolar amount of ethyl acetylacetone. As the reaction proceeds the particles tend to precipitate from solution especially at high concentrations. Therefore, an equally important step of nitric acid addition is necessary to peptize the suspension and keep it stable.

Rather than employ an aqueous solution, alcohol based solutions have improved performances regarding their coating performances [75]. In line with this observation 1-methoxy-2-propanol (Dowanol^{TM}) will be used in the sol solution. The Dowanol^{TM} solvent is preferred for coating since in our project it is readily available and our experience in this solvent's ability to dry evenly is exceptional.

3 High Temperature Strain Gauges

This chapter will cover the process of developing high temperature strain gauges. First the efforts in chemical reduction techniques towards nanoparticles will be explained, then the ink creation process, followed by manufacture and sintering of the final strain gauges.

3.0 Materials

Chromium nanoparticles capped with PVP (40 nm) were obtained from US Research Nanomaterials INC, and were produced by the wire explosion technique. Anhydrous 99.8% pure ethylene glycol, 40 kD polyvinylpyrrolidone (PVP) , ethylenediaminetetraacetic acid (EDTA), palladium nitrate hydrate, 1-methoxy-2-propanol (Dowanol PM), and α-terpineol were sourced from Sigma Aldrich. Glacial acetic acid was bought from Fisher Chemicals. N,N-Dimethylformamide (DMF) was obtained from Caledon Laboratories.

3.0.1 Synthesis:

Typically, 8 mL ethylene glycol, 22 mg chromium nanoparticles, 40 mg EDTA, and 200 mg of PVP were added to a clean and dry three necked flask under a nitrogen environment. 2 mL glacial acetic acid was added to the reaction vessel. The flask was then sonicated for five minutes to disperse the nanoparticles. The flask was then affixed to a schlenk line and stirred at 1000 RPM. In a separate beaker 400 mg palladium nitrate was dissolved in 50 mL DMF. The DMF does not allow the palladium nitrate to form pre-nucleation clusters. The three necked flask was heated to 110°C. The palladium nitrate solution was added dropwise by a syringe pump at 2 mL/hour for 25 hours. The flask was resonicated every 3 hours for 5 min to avoid aggregation of the particles.

After 8 hours of reaction time an additional 8mL of ethylene glycol and 2 mL of acetic acid were added to the reaction to maintain the stability of the reaction. After complete addition, the solution was mixed for an additional hour. A black precipitate was recovered by centrifuging the reaction solution at 8500 RPM for 3 hours.

3.0.1.1 Alternate Synthesis Route

In the previous synthesis route the palladium salt used was the nitrate salt. The synthesis can be modified to use palladium acetate in the following manner.

Typically, 8 mL ethylene glycol, 22 mg chromium nanoparticles, 40 mg EDTA, and 200 mg of PVP were added to a clean and dry three necked flask under a nitrogen environment. 2 mL glacial acetic acid was added to the reaction vessel. The flask was then sonicated for five minutes to disperse the nanoparticles. The flask was then affixed to a schlenk line and stirred at 1000 RPM. In a separate beaker 400 mg palladium acetate was dissolved in 50 mL acetic acid. 1:1 molar ratio of EDTA was added to the solution. The palladium mixture was heated to 60 degrees for a half hour. Excess EDTA was allowed to settle and the resultant dissolved palladium was decanted. The chromium nanoparticle solution was ultrasonically mixed for one minute with the ultrasonic horn at a 50% duty cycle. The chromium and palladium solutions were added to a three necked flask. The three necked flask was heated to 110°C. The mixture was allowed to react for three hours. A black precipitate was recovered by centrifuging the reaction solution at 8500 RPM for 3 hours.

3.0.2 Ink Preparation

The main carrier solvents used for printing are Dowanol PM and α-terpineol. A mixture of 8:1 by volume was used to redisperse the nanoparticles from solution. The nanoparticles were washed

twice by centrifugation in this solution before the final ink was printed. Before printing the ink was sonicated by a bath sonicator for 5 minutes. The ink should remain stable as in Figure 18 below.

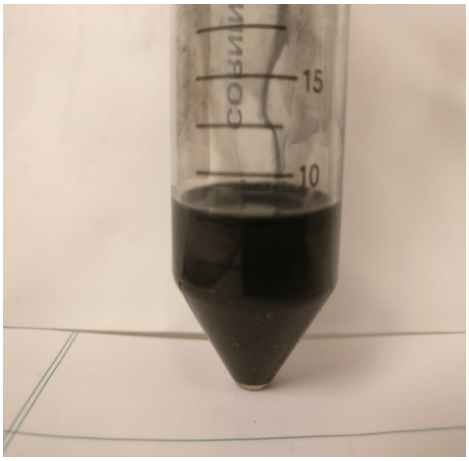

Figure 18 PdCr13 Ink as prepared

Dowanol and α-Terpineol make an excellent solvent for the ink. While the Hansen Solubility Parameters predict that the ink becomes slightly worse to solvate PVP when terpineol is added, the terpineol is required to prevent the coffee ringing effect and as well it provides a non-volatile part of the ink to control evaporation during aersolization.

Table 5 Hansen Solubility Parameters of Ink Components

Component	Dispersion	Polar	Hydrogen
Dowanol PM	15.6	7.2	13.6
α-terpineol	17	5.3	10.9
8:1 Mixture	15.76	6.99	13.3

Polyvinylpyrrolidone	17.4	8.8	14.9

Using a slow polyol process to deposit the palladium on to the chromium allows for the palladium free species to diffuse through the PVP protective layer to cover the particle. However, without care the size of the particles can grow in the micron sized range such as in Figure 19. These particles are not stable in any ink and often crash out during the printing process lowering the amount of solids delivered to the print. The slow process forms dendritic palladium on the surface of the cubes rather than a complete covering.

However, with care to aggregation issues and very slow addition of palladium precursors the desired core-shell particles can be formed as evidenced by TEM EDS in Figure 20. A key to observe here is that the oxygen in the system is diffuse over the surface of the particle whereas uncovered chromium particles always have a high concentration of oxygen around the chromium species when mapped by EDS techniques.

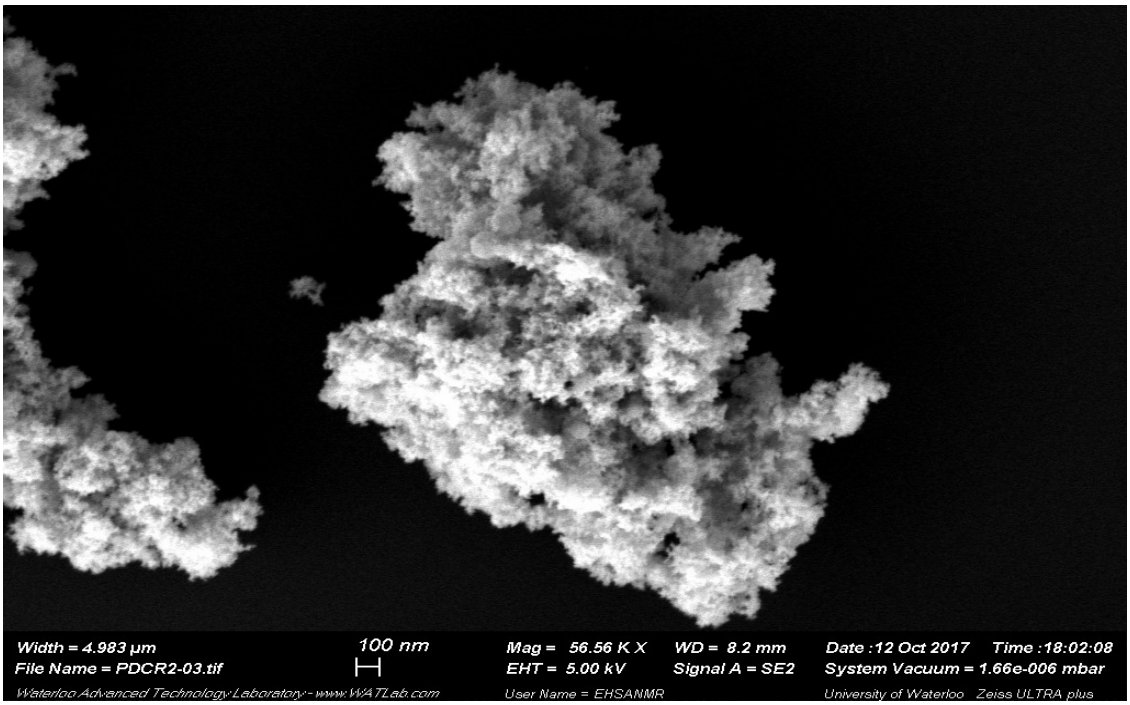

Figure 19 PdCr13 particles with settling problems

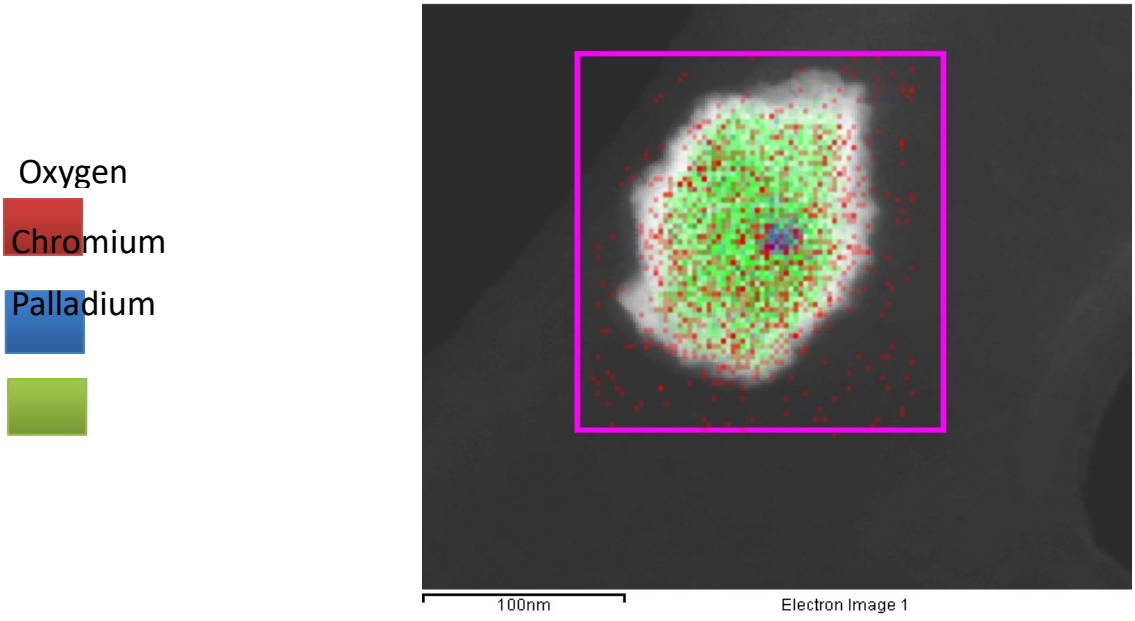

Figure 20 TEM image of particle confirming core shell structure

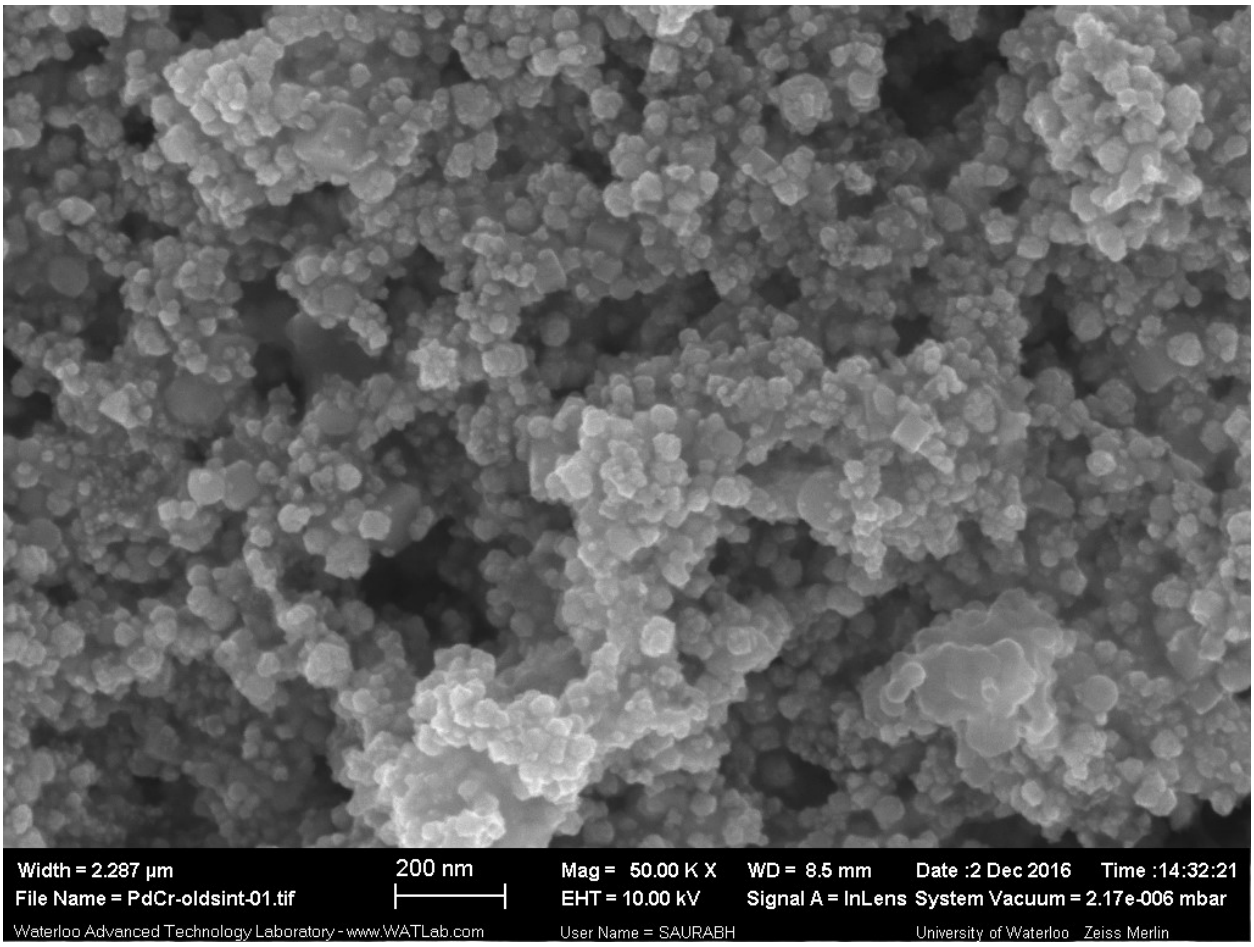

Figure 21 Sintered network of PdCr13 ink showing the sinter necks and chromium particles in the network

The commercial chromium ink formulations allow for the material of PdCr13 to be reliably synthesized and as in Figure 21 sintered together to form a dense percolated track of material for the strain gauges. In sintering the chromium nanoparticles have a higher diffusivity so at temperatures that sinter the palladium the chromium can diffusing into the matrix and form the alloy. The percolated nature of the final material being deposited by these types of inks may also aid strain gauges as the sinter necks give highly strain sensitive scattering centers to the material.

3.1 Results

3.1.1.1 Commercial Chromium Nanoparticles

The raw chromium nanoparticles were characterized as a baseline to demonstrate the instability of the particles and the increased stability of the core shell PdCr13.

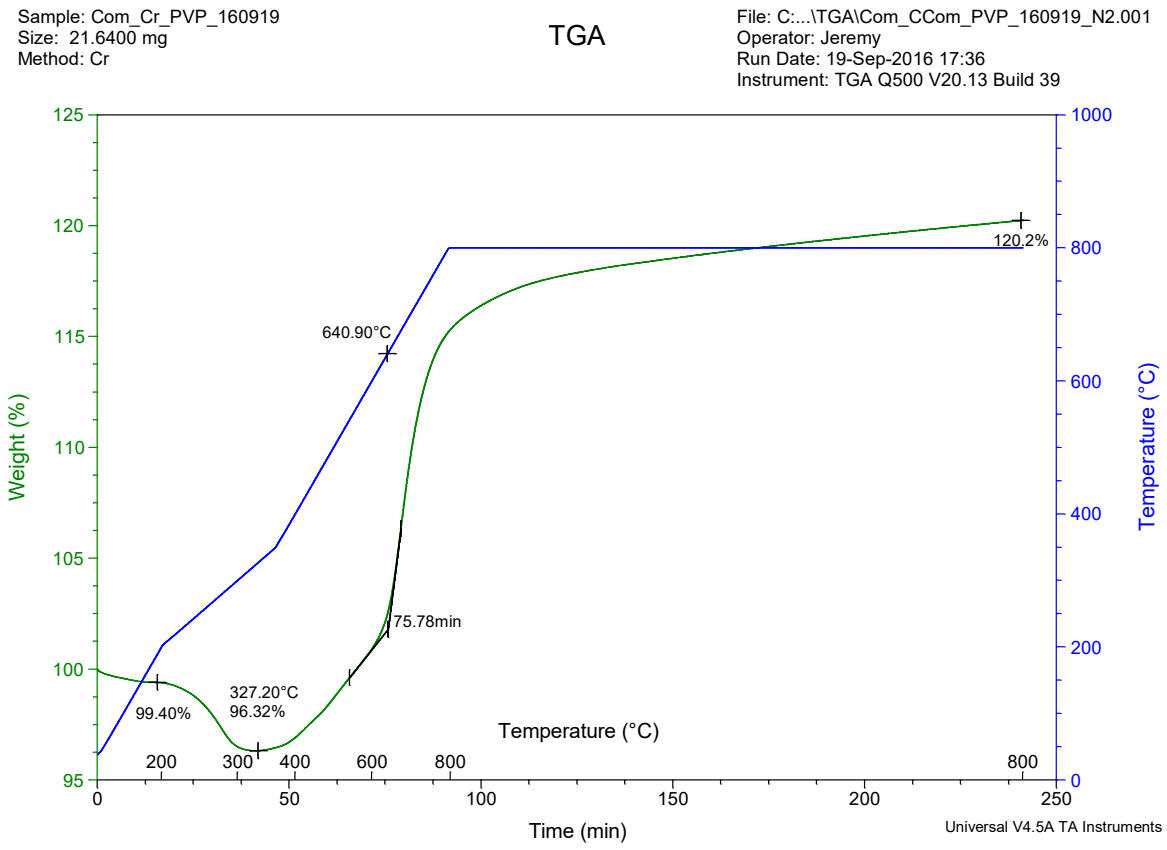

Figure 22 Oxidation of commercial nanoparticles in nitrogen

The TGA is useful mainly in polymer and corrosion studies making it very suitable for testing high temperature strain gauge materials. The first stage tracks the thermal degradation of the polymer used to cap the nanoparticle. The second stage monitors the metal left behind for any mass gains

from either oxygen or nitrogen reactions. Additionally, in atmospheres of nitrogen or oxygen and at high enough temperatures complete conversion into the most thermodynamically stable oxidized state can be assumed. From these mass gains the actual content of chromium can be calculated assuming that the palladium does not react at these temperatures.

The mass change from the bottom to the peak in TGA curves gives the amount of nitrogen or oxygen gained by the material. The amount of chromium in the unoxidized state is given by:

$$\frac{mass_{cr}}{mass_{initial}} = \frac{M_{Cr}}{M_{impurity}} * \Delta m + mass_{capping} \quad \text{Equation 27}$$

For nitrogen rich environments conversion into CrN would follow Equation 28.

$$\%Cr = \frac{52}{14} * \Delta m + mass_{capping} \quad \text{Equation 28}$$

In oxygen containing environments Cr_2O_3 is formed and the mass gain can be given from Equation 29.

$$\%Cr = \frac{104}{48}\Delta m + mass_{capping} \quad \text{Equation 29}$$

In the experiments that follow Equation 29 has been used in all the calculations as elemental analysis has shown that even in pure nitrogen streams in the instrument the trace oxygen contaminants react preferentially to form the oxide over the nitride.

From Figure 22 we can follow the equations as follows for a sample calculation. The assumption will be that CrN was formed from the nitrogen atmosphere. The Δm from the point where the polymer was removed was 23.88% and the mass polymer removed was 3.9% . So as follows:

$$\%Cr = \frac{52}{14} * 23.88 + 3.9$$

$$\%Cr = 88.7\% + 3.9\%$$

$$= 92.6\%$$

Equation 30

An estimate from the mass gain reveals that the compound contained 93% active chromium as purchased. This means that 7% of the original particles consisted of amorphous chromium impurities. If oxygen impurities are present this would have inflated the active chromium calculation. To compare we also performed this test in a regular atmosphere:

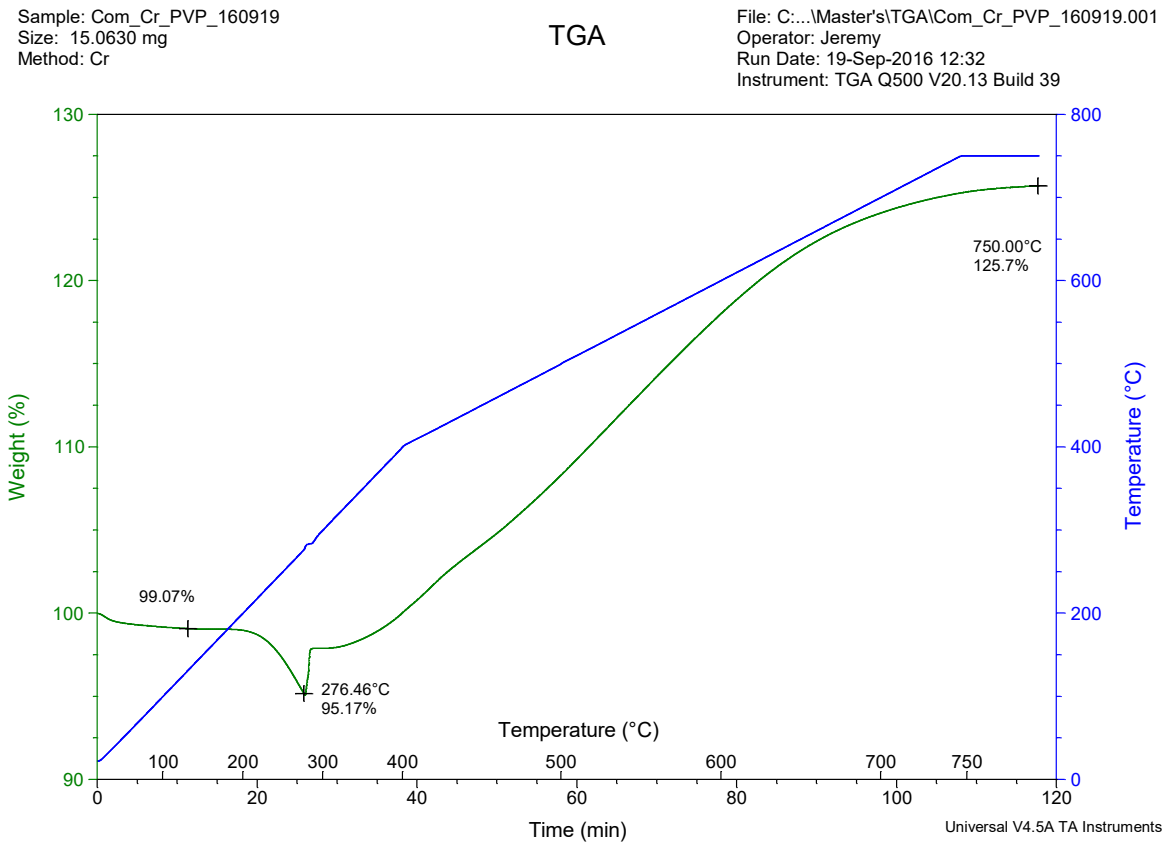

Figure 23 Oxidation of commercial nanoparticles in air environment

These results tell of a system that contains 70% active chromium where nitrides will have caused this result to be lower. Using these tests as a baseline the active chromium content in the chromium nanoparticle is anywhere between 70-90%. So while these particles are the most pure that this project could obtain there still exists some oxidized materials in the final ink as produced.

The mass gain in each of the graphs start indicating when the chromium starts to react with the atmosphere. Interestingly this mass gain starts immediately and rapidly after the decomposition of the capping layer. The decomposition of the PVP on the particles occurs between 200-300˚ C

whereafter in nitrogen there is a slow mass gain till 640 ˚ C and in oxygen this mass gain occurs immediately at 275 ˚ C.

3.1.2 Role of additives in synthesis

The additives in the synthesis of the nanoparticles were necessary to alter the reaction thermodynamics and kinetics. The palladium salts would decompose at room temperature. The palladium nitrate would decompose into palladium oxides in water and alcohols. Palladium acetate would decompose into palladium metal particles in in alcohols. The EDTA additive prevented the decomposition of the palladium acetate in alcohols by forming palladium EDTA complexes in acetic acid. The palladium binds preferentially to the EDTA and stabilizes the compound. The acetic acid was used as it was found to be an excellent solvent to suspend the chromium nanoparticles in as the suspensions were stable for up to 24 hours.

3.1.2.1 PdCr13

TGA on the core shell PdCr13 particles reveals material information as well as the degree of oxidation hindrance the shell applies to the particles.

Figure 24 shows the mass gain from the atmosphere on the particles. The oxygen tests have proven to be the most reliable in gauging the chromium content as these tests will not be affected by the chromium intermetallic that interfere in x-ray techniques. The mass gain between 400 and 600˚C tracks well with Cr_2O_3 formation. As well it the intermetallic formed become unstable and volatile after 750 ˚C.

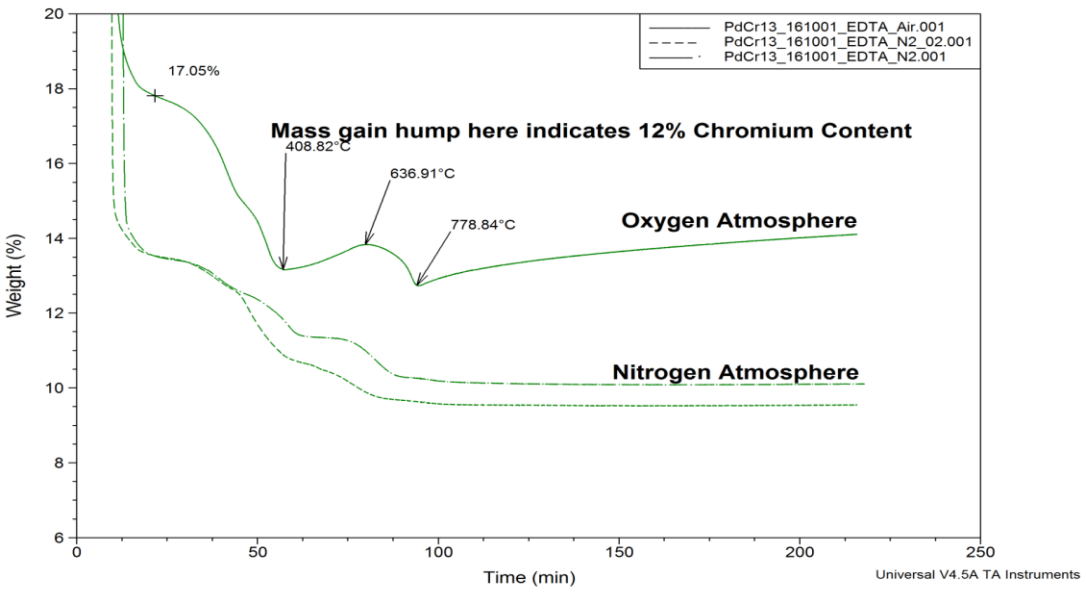

Figure 24 PdCr13% Elemental Analysis by mass gain

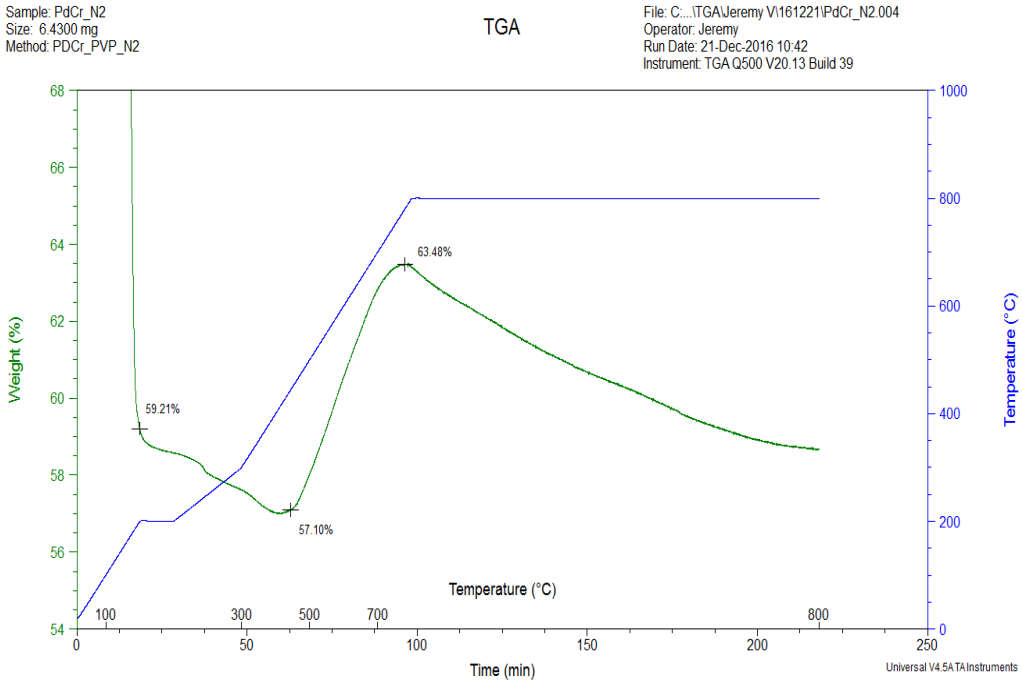

Figure 25 Delayed oxidation in the PdCr13 system

When the palladium shell is added to the chromium system, the onset of the oxidation in nitrogen is delayed from 330˚C in Figure 22 to just above 400˚C in Figure 25. However, after this delay the oxidation occurs as rapidly as before. This delay shows the increased diffusion time for the chromium to go through the palladium shell. During sintering this increased protection allows for the vaporization of the organic compounds with decreased concerns of the chromium reacting with the free carbon before the carbon can react with the atmosphere and become a gas.

3.1.3 Size Distribution

Measuring the size distributions of the particles is another method the can be used to confirm the core-shell structure of the particles. By example in Figure 26 the shift in the size of the particles indicates that the the palladium deposits on the chromium. If nucleation steps had occurred there would be a bimodal distribution of particles. The size is a problem though as the distribution has quite a number of particles over the 100 nm limit for aerosol inkjet printing.

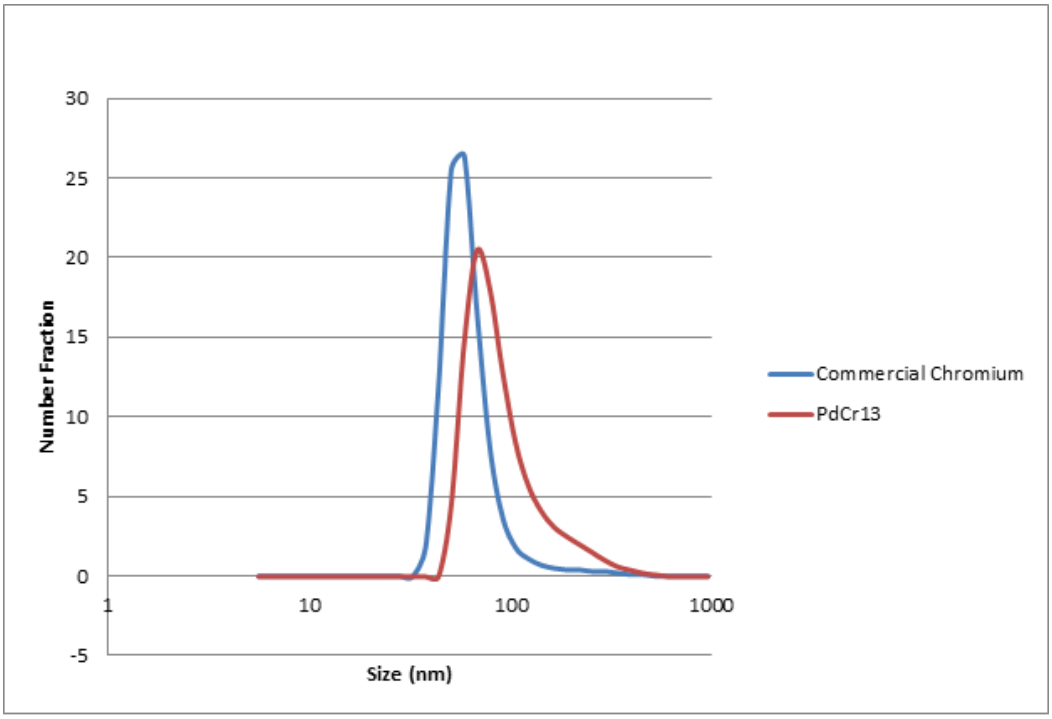

Figure 26 Size Distributions of the original chromium nanoparticles and the PdCr13 particles. The average sizes of the particles were 65nm and 98 nm respectively. Calculated from DLS results.

To resolve the size issue further work will have to be done to either reduce the size of the starting chromium nanoparticles or investigate bimodal mixtures of inks where some of the palladium exists as smaller particles and not as a shell on the surface of the chromium.

3.2 Printing

Though the size of the particles remains an issue work was performed on printing the formed ink in the aerosol ink jet printer. The parameters of each print were determined at the beginning of the print. The ink as formed typically had to have some modifications to it before it was able to be printed. The most common modifications were alterations to the surface tension of the ink because the surface tension was either too low or too high. If excess capping agent remained in the ink

often PVP's ability to act as a surfactant lowered the surface tension of the ink to the point where aerosolization did not occur. Otherwise if not enough high temperature solvents such as terpineol the droplets after aerosilization would vaporize to too small of a radius that the stokes number would decrease below one and the material would not deposit on the substrate.

When the printer would be operating nominally a track width of 20-30 microns would be deposited as in Figure 27. The larger particles in the ink are deposited at the center of the track where as the smaller particles follow the airflow divergence at the surface of the substrate and tend to form the overspray of the material.

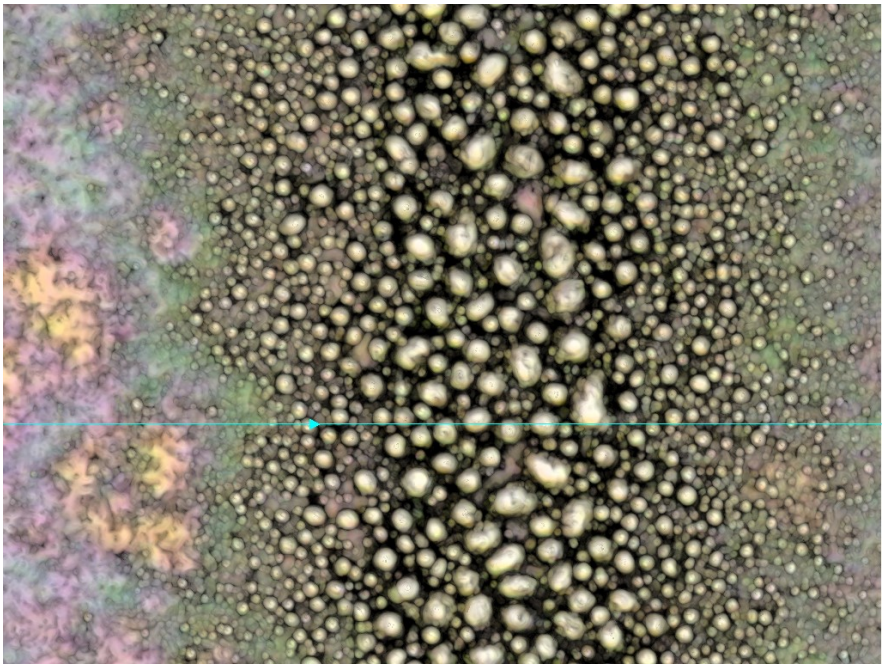

Figure 27 Track of PdCr13 printed at a width of 30 um

The ink is stable in the printer over the course of a few hours. Periodically the ink must be sonicated in a ultrasonic bath to break up any aggregates that have formed in the printing vial.

The strain gauge is formed by printing individual lines of ink to form the pattern of the strain gauge in Figure 28 below. Typically the thickness in one pass of the printer depends on the amount of aerosol being generated in the chamber. The amount of material typically prints in the 200-1000 nm range in a print. As such to form a percolated strain gauge multiple passes have to be made.

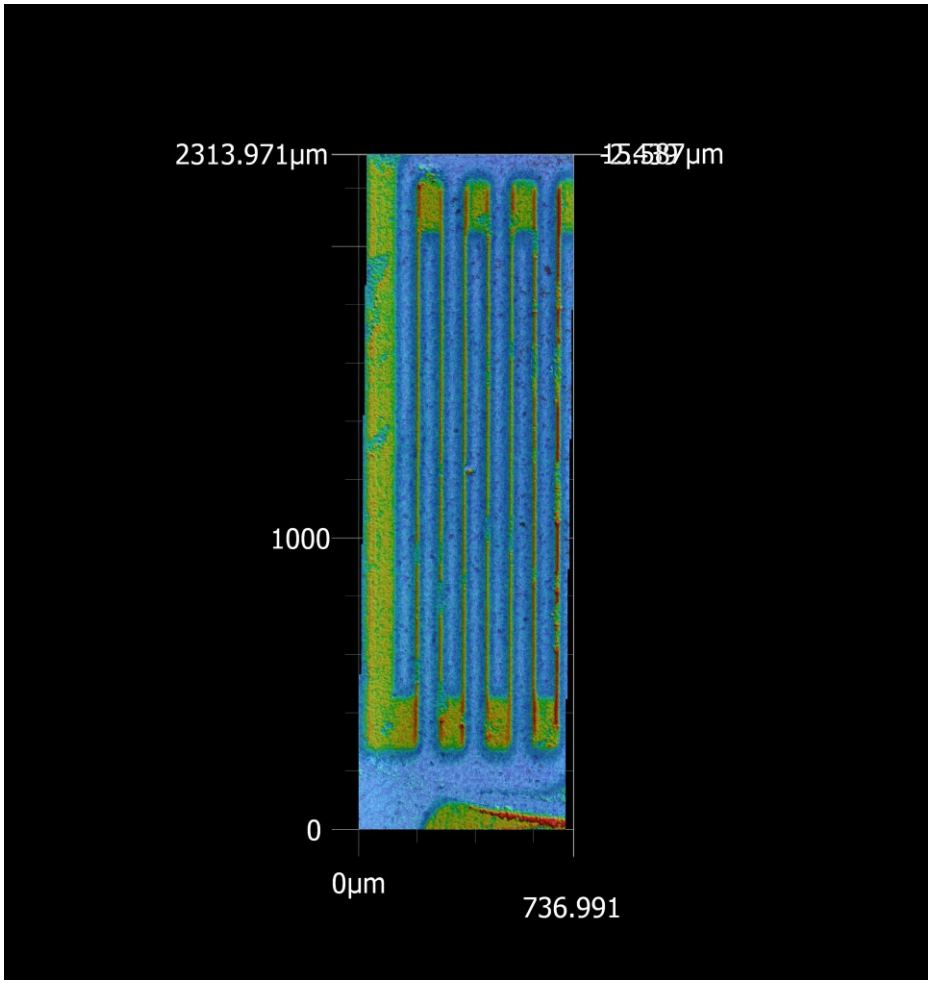

Figure 28 Printed strain gauge

When making multiple passes the layer underneath should have most of the solvent evaporate before a new layer is applied, this may be a problem with some of the inks developed since the

solids content is typically at 5% so there is gross solvent drying occurring on the substrate after the print has occurred.

In printing the ink, a variety of process parameters work for deposition. The flow ratio used between the delivery stream and the focusing stream is typically between 1.5-2.5. The aerosol is also heated in the delivery system to 80˚C and the substrate to 100˚C to aid in solvent evaporation and densification of the pattern. To control the amount of material being deposited the delivery stream is fixed to 20 ccm of flow and the speed of the printing is altered to increase or decrease the thickness being printed.

The optimization of the printing will occur in later stages of the project as the ink development is standardized.

3.3 Sintering

The next stage in the progress to convert PdCr13 ink into a high temperature strain gauge is the sintering process. Sintering is the process where the small particles are heated enough that the diffusion of the atoms allow the particles to join to create a complete network like in Figure 29. Prior to the diffusion process the sintering process removes the capping layer on nanoparticle through thermal decomposition. Controlling the heating rate and the atmosphere at this stage is important. Not enough heat and the diffusion process is prohibitively slow but too much will cause side reactions with the atmosphere or cause the necks of the particles to break away from each other.

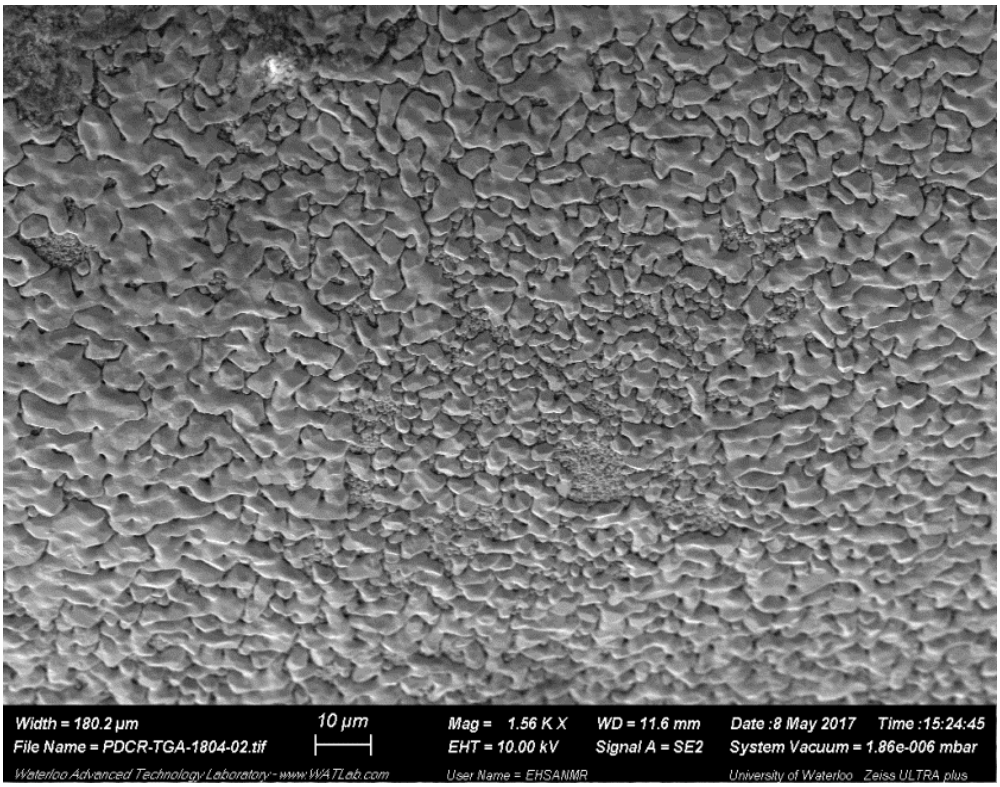

Figure 29 Drop Cast Sintered ink

To produce a conductive network with the PdCr13 ink the following sintering procedure has been followed:

1) Under a 5% hydrogen environment in a tube furnace conduct the following heating rates
2) A slow 1˚C/min heat ramp from room temp to 200˚C to remove any solvent
3) Increase ramp to 2˚C/min to 750˚C to remove the capping agents and to begin sintering the particles
4) Hold at 750˚C for one hour to allow sintering process to occur.
5) Cool at 2 ˚C/min to room temperature.

Pure argon environments screened to sinter the inks but conductivity was elusive with this atmosphere because trace amounts of oxygen in the gas stream reacted with the material at high temperature. The hydrogen environment ensures that any such contaminants are reduced and helps revert any chromium oxide that may be present in the printed pattern.

Above 750 ˚C the patterns lose their conductivity due to material loss that was observed in the TGA study.

3.3.1 XRD

The sintering study has also been aided by XRD techniques as well. XRD allows the direct analysis of the crystal structures involved. In Figure 30 different samples sintered in differing conditions are presented. The peaks of palladium are present in each sample. The higher temperature argon sample has a slight amorphous peak around 20˚C which indicates that there are some amorphous intermetallics present. This peak is more pronounced in the sample sintered at a lower temperature, which confirms that the intermetallic species have yet to volatize. In the hydrogen atmosphere the broad peak disappears while the peaks of the palladium greatly reduce in intensity. The reduction in intensity occurs most likely from the palladium grains diffusing into each other during the sintering process.

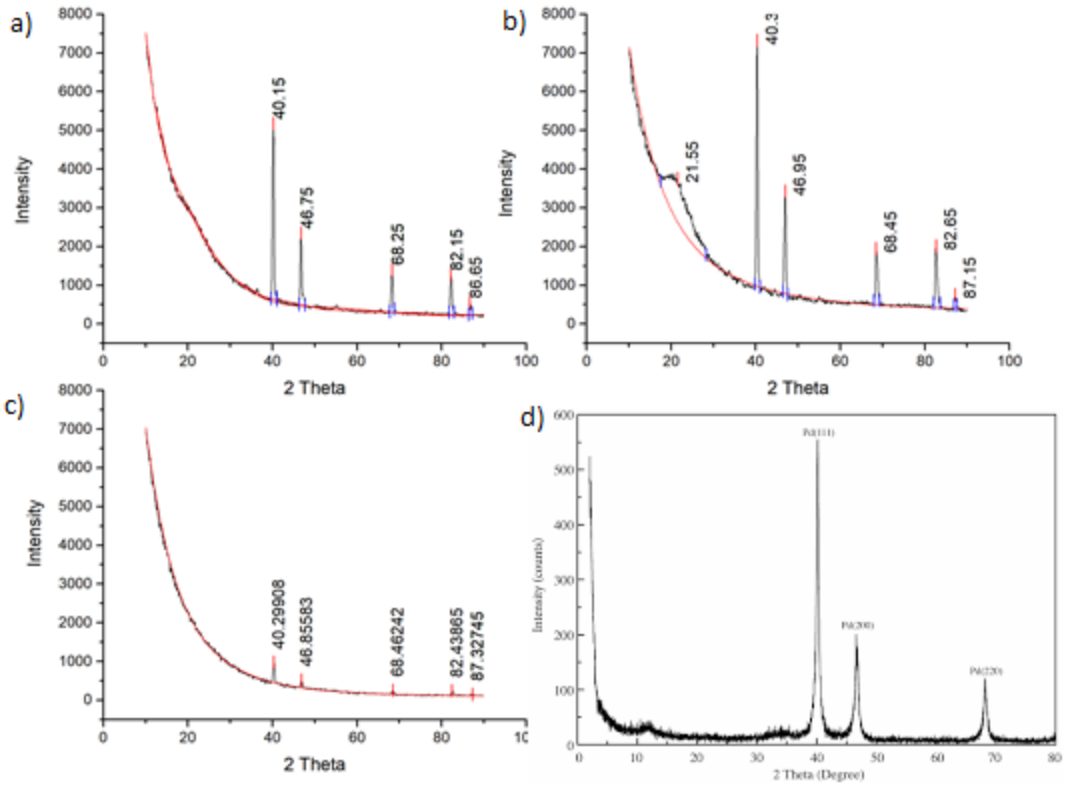

Figure 30 XRD Patters of PdCr13 Ink sintered under differing conditions. a) Upper left sintered at 1000 C in argon atmosphere b) Upper tight sintered at 750 C in Argon c) Sintered in 5% hydrogen in argon at 750 C d) typical palladium XRD peaks

3.4 Electrical measurements

Though preliminary, some gauges were tested for their resisitive responses or R_0 for their eventual use as a strain gauge. The measurements were performed with a microprobing station.

The resistance of a three fingered gauge came to be 31 kΩ from the results in Figure 31. Additional I-V curves can be found in Appendix A.3. The resistance is linear with some deviance around zero due to measurement error. The resistance is quite high for a metal based device. The high resistance is explained by the sintered and resistive nature of the materials employed. Future work will

attempt to bring down the resistance of the strain gauges by improving the material densification and removing the impurities and side reactions that occur during synthesis and processing.

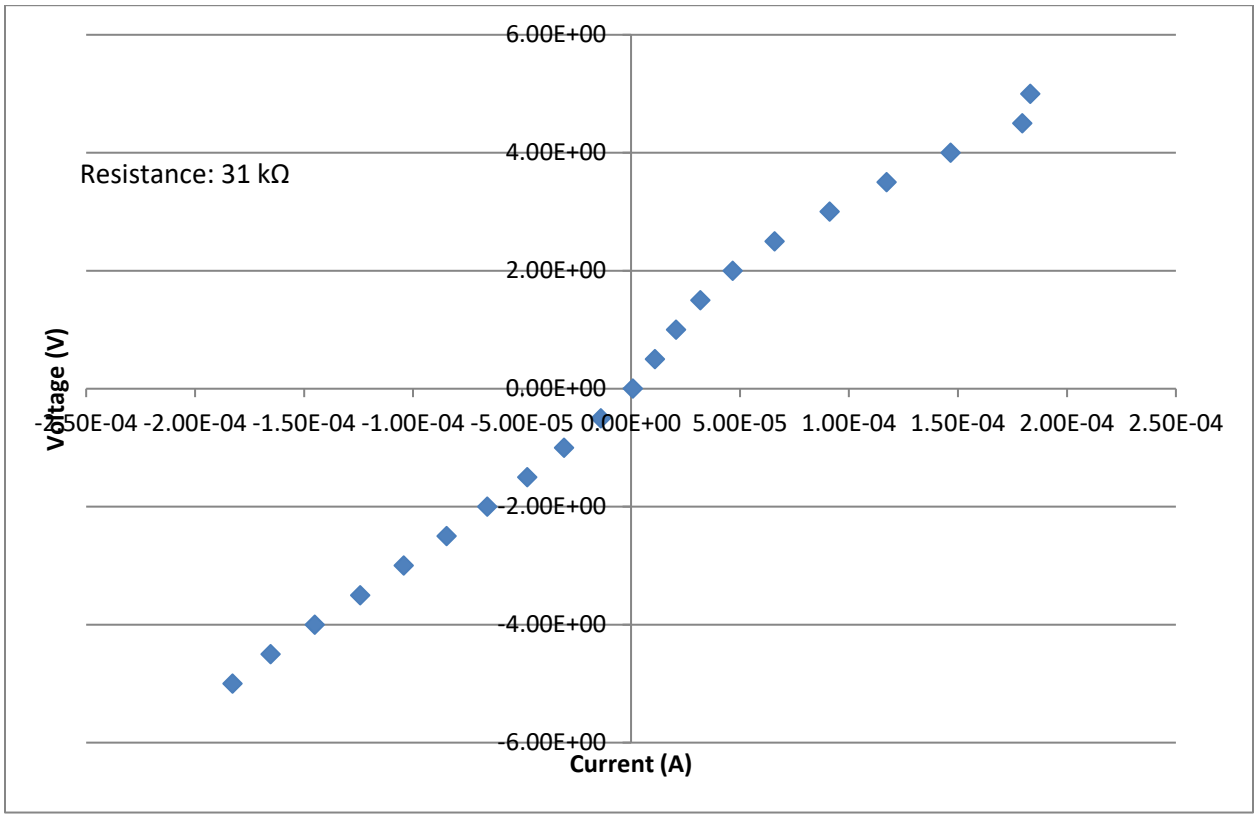

Figure 31 Resistance of a test strain gauge under no loading

3.5 Summary

In summary a palladium chromium alloy nanoparticle ink for aerosol ink jet printing has been prepared as a preliminary study into the development of high temperature strain gauges produced by additive manufacturing. The inclusion of chromium in the solution was not avoidable and presented most of the challenges encountered in the process. By chemically reducing a shell of palladium on the chromium seed produced by wire explosion the ink was developed. The ink was able to be printed, sintered and electrically tested. While the material itself is not stable up to the

desired 1000˚C, it is the most stable material that could be developed for this purpose. The additional temperature requirements will come from the packaging of the sensor with protective inert coatings which the next chapter covers.

4 Sol Gels

The sol gel process was developed with the intension of producing a protective coating to both the substrate that would be printed on and as an encapsulation coating to prevent oxidative attack on a high temperature sensor. The sol gel technique produces ceramics via wet chemistry and was attractive to avoid the costly and long turnaround commercial coatings from GE Aviation.

The sol-gel process is a very common procedure for making ceramic powders. The technology has its roots all the way back to 1842 [81]. The technology was not a success at first because the film aging time was in the range of a year to avoid mechanical defects. In the late 20th century these issues were resolved by a host of researchers in order to develop a library of materials that could be processed by the sol-gel technique[69], [71], [82]. Much of the work has been based off of silica based gels but the technique is flexible to cover any metal oxide. There are a couple excellent reviews on this technology regarding metal protection with sol-gel films[16], [79].

The name of the process basically defines the components of the technology. A ‘sol’ is prepared such that a gel is eventually formed by curing the sol. The ‘sol’ refers to the suspension of particles in one of the intermediate steps. The gel is the processible phase of the material. The technique described converts a metal alkoxide solution into a xerogel film and anneal into a dense film.

4.0 Materials and Methods

With sol-gel formulations having been used as precursors for forming ceramics since 1970 [69] there exists few new contributions; however the early inventions concerned themselves with producing porous ceramic powders for substrates in catalysis and the like [70], [71]. The problem with forming dense continuous films is due to the shrinkage incurred during the drying and curing stages in the sol-gel process [73]. The following method overcomes the shrinkage issues by adding predensified alumina nanopowders to the sol after formation.

The flow of the reaction is as follows:

1) Aluminum Sec-but-oxide is mixed with Dowanol in a concentration of 0.4 M. This mixture is stirred at 80°C for a half hour. This allows for the hydrolysis reaction to proceed. The hydrolysis is a fast reaction that rapidly gels the solution. The prolonged heat rate allows the gel to relax back into a clear solution.
2) Next Acetylacetone is added in an equimolar ratio to terminate the hydrolysis reaction and stabilize the sol for storage. The Acetylacetone chelates the particles protecting the hydroxide functional groups that surround the particles. The solution is maintained at 80°C for an additional half hour.
3) Glacial acetic acid is added to peptize the solution. $1/5^{th}$ of the reaction volume should be added as acetic acid. The solution is heated to 105°C for two hours. At this point the particles visibly precipitate.
4) Addition of nitric acid in a small volume is added until the pH of the solution becomes acidic. The sol-gel buffers this addition and the pH will remain stable until it rapidly

changes as the solution peptizes. This is the act of changing the surface charge of the suspended particles.

5) The above solution is added as 10% volume to a 20% wt solution of alumina nanoparticles suspended in water. This allows significant shrink prevention as 90% of the solids will already be condensed. The nanoparticles also act as nucleation sites for the sol to start a film formation.
6) The as formed sol is destabilized in mixing with the nanoparticles. Appropriate small additions of nitric acid (<1mL) resuspend the sol and allow for uniform coating without aggregates.

The produced solution is directly used after sonication in a modified dip coating procedure. To enable the dip coating the linear stage on a mechanical tester was employed as pictured in Figure 32 and Figure 33. The process involves a few key steps. The substrate to be coated is slowly submersed in solution avoiding air bubble entrapment that may disrupt the film. After each coat the substrate is heated to at least 500˚C to semi-cure the bottom coat and remove the solvents before application of additional coats. During the coating process 1.5V is applied between the substrate and the bath as this allows the sol particles in solution to migrate to regions of high electric field density which are the corners of a substrate. This migration offsets dipcoating's tendency to create thinner films at the edges of substrates.

Figure 32 Top: Sol-Gel coating through an enhanced dip coating procedure

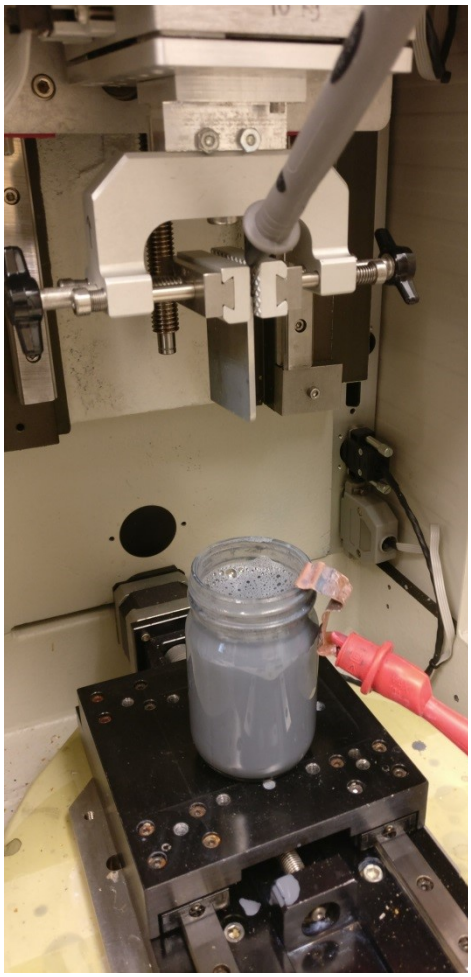

Figure 33 Right: Dip coating set up, on an motorized x,y,z stage

4.1 Sintering

Once sufficient thickness was achieved with the coating procedure the films underwent a final sintering stage where the sol gel continued to cure and densify. Alumina goes through different phase transformations as the temperature is increased. The most stable form that is the dense form needed for the protective applications is called the alpha phase. According to the phase diagram of

alumina a gel goes through the eta, theta and alpha phases as per Figure 34. To reach the alpha phase the temperature must be raised above 1300 K. This 1300 K is the temperature limit for the high temperature strain gauges so it is necessary for the coat to be cured at this temperature.

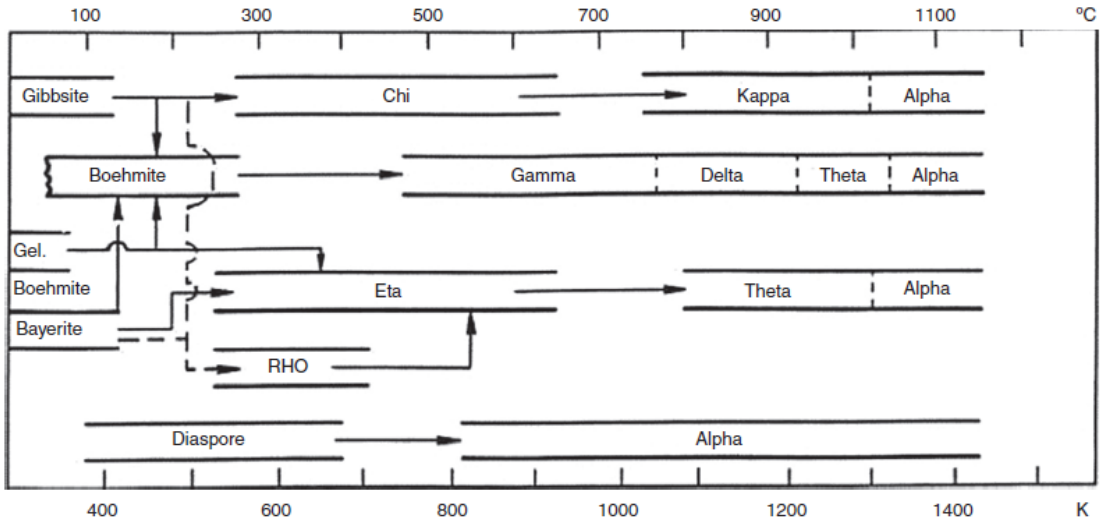

Figure 34 Phase transformations of alumina from a sol-gel. [83]

Sintering of the films occurred in regular atmospheric conditions allowing oxygen to freely react and burn off the organics and hydrides in the gel. Typical sintering temperatures were in excess of 1000˚C and below 1300˚C as the substrate used started to warp above those temperatures.

4.2 Coating Performance

Once formed the sol-gel films formed a dense electrically insulating film. The film was lighly scratch resistant but pressure from a sharp point such as an electrical probe would puncture the film. Figure 35 and Figure 36 depict a typical film after sintering. When imaged by SEM the film would glow due to charge build up but defects in the film such as holds would show up dark against the film as these would be conductive pathways for the electrons. The films were smooth and could

be applied to surfaces with roughnesses lower than 10 um, which is superior to other film processes for these techniques which often need to be polished below 1 um roughness.

Figure 35 Scanning electron microscopy of a sol-gel coating demonstrating the insulation by charge buildup

Figure 36 Close up view of damaged hole in Figure 35 revealing the damage

4.3 Raman Investigation

To further compare the produced coatings to the coatings commercially provided, raman spectroscopy was performed. Raman analyzes the shift in wavelengths in light emitted from a substance. The shifts looked at come from the energy adsorbed by the vibrations electronic cloud. As such each compound has its own fingerprint of raman radiation provided that the substance has a polarizable electronic cloud. Most ceramics can be analyzed this way.

In Figure 37 the different coating are analyzed. The commercial coatings have the appropriate broad peaks for alumina being present. The sol-gel solution also contains these peaks but with a strong peak at 1400 cm^{-1}. These peaks continue to exist in the sol-gel coatings and correlate to the alumina intermetallics. The peaks from the alumina around 600-800 cm^{-1} are also diminished possibly due to a lack of crystallinity in the films as deposited.

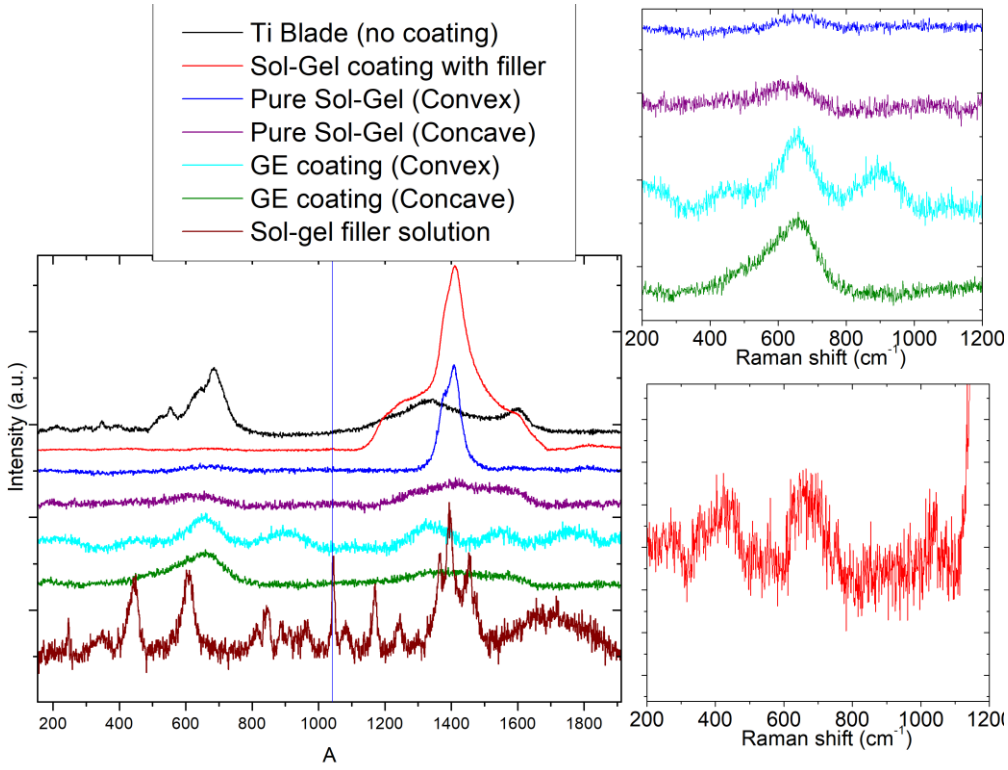

Figure 37 Raman analysis of as deposited sol-gel coatings

4.4 Adhesion

An additional concern to the sol-gel process is that the bonding to the substrate has become an issue. Since the sintered alumina particles do not present a full surface to bond with the metal substrates underneath the interface between the two becomes a weak point in the strain gauge application. In Figure 38 the stresses caused by the strain gauge being sintered on top of the alumina sol gel actually delaminates the sol gel from the substrate which is visible underneath. As such additives to the gel to increase this adhesion will be considered in future work. This problem may be avoided by using processes that put less stresses on the film during production.

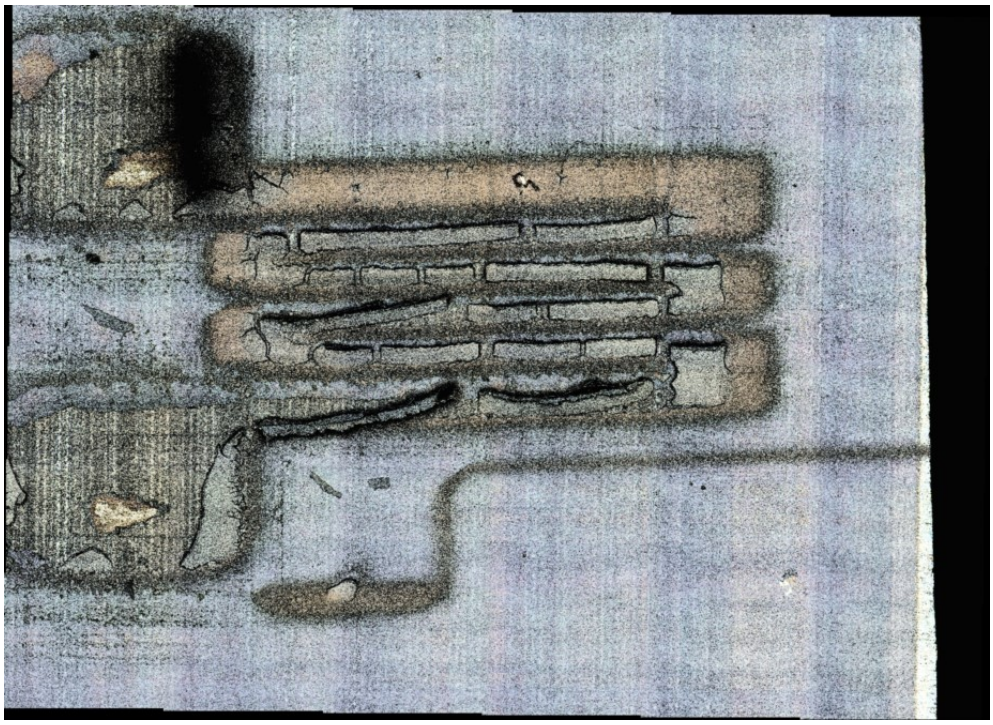

Figure 38 Delamination of a printed substrate

4.5 Future Work

The sol-gel process in combination with additive manufacturing may prove to be very useful as a wet chemical technique can easily be adapted to use with the aerosol ink jet printer to deposit these films locally rather than have to be deposited by dip coating or other film deposition techniques. The sol-gel process allows exact control over the chemical composition of the material being deposited, with this in mind much like in high temperature corrosion, additives to enable self healing in the form of nanoparticles will also be considered. This may help with the densification issues and help resolve the adhesion if the correct additives are considered. When established the

sol-gel technique will also help encapsulate the strain gauges to provide an inert film to cover the oxygen sensitive materials in high temperature sensor applications.

5 Conclusion and Recommendation

This thesis sets the ground work for materials intended for additively manufacturing strain gauges that operate at 1250K. The nanoparticles were produced and suspended in an ink for this purpose. The ink was subsequently printed with aerosol ink jet printing and sintered into a conductive strain gauge. The promise of high temperature performance had yet to be realized due to the difficulties with the corrosion and stability of the alloys used. Additionally, sol gel materials were applied to the surface of tested parts to act as an insulation layer between the conductive substrate and the gauges. The method shows a unique ability to create this insulation layer on rougher surfaces than previous methods. Sol gels exist as a wet chemical method they are readily suitable for being able to be printed by the aerosol ink jet printer. This allows for localized placement of insulation layers and even functionally graded encapsulation layers if desired.

I would recommend that this work continue forward with new materials and methods to avoid corrosion of the sensor at these temperatures. Thermal experiments have shown that the chromium nanoparticles are unstable at elevated temperatures. The core shell formulations stabilize these nanoparticles to make them more stable during subsequent processing phases. Appropriate nanoparticle inks can be made for conductive applications by starting with precursors that do not contain impurities that may react with the metals during the sintering process. The inks that can be created for aerosol ink jet printing must mimic the liquid properties of water yet avoid the formation of hydroxides to realise these goals. Sol-gel technology also gives a promising route to deposit dense ceramic films via wet chemistry. The density of the films were improved by adding ceramic particles that were already annealed to the alpha alumina phase. Sensors encapsulated by insulating ceramics remove the need for the material to be able to grow its own protective oxide

allowing greater design freedom with maintaining stable electrical performance from the strain gauge.

5.0 Future Work

The future work planned for this project is to improve the consistency of the strain gauges after printing and sintering. The goal is to be testing the gauges for dynamic responses as well as stress testing them at elevated temperatures. To reach this goal new materials may have to be considered. Of crucial importance is the encapsulation of the devices to protect the strain gauges from corrosion in the environment as often the native oxide is insufficient. As well work with the adhesion of the gauges will be investigated as part of this encapsulation step. It is the aim of this work that sol gel technology can enable additive methods to apply the encapsulation layer to manufactured parts. These methods are in demand because aerosol ink jet printing can place strain gauges at places that are inaccessible to today's technology.

Works Cited

[1] E. Jabari and E. Toyserkani, “Micro-scale aerosol-jet printing of graphene interconnects,” *Carbon N. Y.*, vol. 91, pp. 321–329, Sep. 2015.

[2] T. Seifert, E. Sowade, F. Roscher, M. Wiemer, T. Gessner, and R. R. Baumann, “Additive manufacturing technologies compared: Morphology of deposits of silver ink using inkjet and aerosol jet printing,” *Ind. Eng. Chem. Res.*, vol. 54, no. 2, pp. 769–779, 2015.

[3] R. Eckstein, “Aerosol Jet Printed Electronic Devices and Systems,” 2016.

[4] H. Liu, S. Jiang, X. Zhao, H. Jiang, and W. Zhang, “YSZ/Al2O3multilayered film as insulating layer for high temperature thin film strain gauge prepared on Ni-based superalloy,” *Sensors Actuators, A Phys.*, vol. 279, pp. 272–277, 2018.

[5] E. Jabari and E. Toyserkani, “Aerosol-Jet printing of highly flexible and conductive graphene/silver patterns,” *Mater. Lett.*, vol. 174, pp. 40–43, 2016.

[6] J. Ward, C. Hardwicke, J. Lomas, Eminoglu, and T. Reld, “Selective Localized Coating Deposition Methods and Systems for Turbine Components,” US 2016/0047253 A1, 2016.

[7] J.-F. Lei and H. A. Will, “Thin-film thermocouples and strain-gauge technologies for engine applications,” *Sensors Actuators A Phys.*, vol. 65, no. 2–3, pp. 187–193, 1998.

[8] S. Kasap, C. Koughia, and H. Ruda, “Electrical Conduction in Metals and Semiconductors,” in *Springer Handbook of Electronic and Photonic Materials*, Springer, 2017, pp. 19–45.

[9] J. D. Wrbanek, G. C. Fralick, and G. W. Hunter, “Thin film ceramic strain sensor development for harsh environments,” 2006.

[10] A. . Fallis, “Turbine Engine Hot Section Technology 1986,” in *National Aeronautics and Space Administration*, 1986.

[11] M. J. Renn, B. H. King, M. Essien, G. J. Marquez, M. G. Giridharan, and J.-C. Sheu, “APPARATUSES AND METHODS FOR MASKLESS MESOSCALE MATERIAL DEPOSITION,” US 7,485,345 B2, 2009.

[12] K. Taneichi, T. Narushima, Y. Iguchi, and C. Ouchi, “Oxidation or Nitridation Behavior of Pure Chromium and Chromium Alloys Containing 10 mass%Ni or Fe in Atmospheric Heating,” *Mater. Trans.*, vol. 47, no. 10, pp. 2540–2546, 2006.

[13] C. Lee, N. R. Kim, J. Koo, Y. J. Lee, and H. M. Lee, “Cu-Ag core-shell nanoparticles with enhanced oxidation stability for printed electronics.,” *Nanotechnology*, vol. 26, no. 45, p. 455601, 2015.

[14] M. J. Kammer, A. Muza, J. Snyder, A. Rae, S. J. Kim, and C. A. Handwerker, “Optimization of Cu – Ag Core – Shell Solderless Interconnect Paste Technology,” vol. 5, no. 7, pp. 910–920, 2015.

[15] C. Jing, X. Zhao, and Y. Zhang, “Sol-gel fabrication of compact, crack-free alumina film,” *Mater. Res. Bull.*, vol. 42, no. 4, pp. 600–608, 2007.

[16] M. Zheludkevich, I. Salvado, and M. Ferreira, “Sol–gel coatings for corrosion protection of metals,” *J. Mater. Chem.*, vol. 15, no. 1, pp. 5099–5111, 2005.

[17] B. Hu, M. Yao, P. Yang, W. Shan, and X. Yao, “Preparation and dielectric properties of dense and amorphous alumina film by sol-gel technology,” *Ceram. Int.*, vol. 39, no. 7, pp. 7613–7618, 2013.

[18] C. Goth, S. Putzo, and J. Franke, “Aerosol Jet printing on rapid prototyping materials for fine pitch electronic applications,” *Proc. - Electron. Components Technol. Conf.*, pp. 1211–1216, 2011.

[19] B. L. Tong and J. Guo, “Noble Metal Alloys as Strain Gauge Materials,” *Platin. Met. Rev.*, no. 3, pp. 98–108, 1994.

[20] D. E. Sokolowski and C. R. Ensign, “Turbine engine Hot Section Technology (HOST) project,” in *NASA report*, 1985.

[21] E. Y. Garcia and D. G. Loffler, “Electrical resistivities of iridium, palladium, rhodium, and tungsten at temperatures between 295 and 1100 K,” *J. Chem. Eng. Data*, vol. 30, no. 3, pp. 304–305, 1985.

[22] C. O. Hulse, R. S. Bailey, and F. D. Lemkey, “HIGH TEMPERATURE STATIC STRAIN GAGE ALLOY DEVELOPMENT PROGRAM,” NASA, 1985.

[23] N. P. Neumann and Venkatraman, “The Cr-Pd (Chromium-Palladium) System,” *Bull. Alloy Phase Diagrams*, vol. 11, no. 1, pp. 11–15, 1990.

[24] K. Taneichi, T. Narushima, Y. Iguchi, and C. Ouchi, “Oxidation or Nitridation Behavior of Pure Chromium and Chromium Alloys Containing 10 mass%Ni or Fe in Atmospheric Heating,” *Mater. Trans.*, vol. 47, no. 10, pp. 2540–2546, 2006.

[25] J. D. Wrbanek, G. C. Fralick, J. Wrbanek, and G. Fralick, “Thin Film Ceramic Strain Sensor Development for High Temperature Environments,” 2008.

[26] J. R. Rumble, Ed., “‘Electrochemical Series,’” in *CRC Handbook of Chemistry and Physics 98th Edition*, 98th ed., Boca Raton, FL: CRC Press/Taylor & Francis, 2018.

[27] N. L. Pacioni, C. D. Borsarelli, V. Rey, and A. V Veglia, *Silver Nanoparticle Applications*. 2015.

[28] M. G. Barak R Lomax, "REACTION MECHANISMS OF THE HYDRAZINE ELECTRODE."

[29] D. D. M. Wayner, D. J. Mcphee, and D. Griller, "Oxidation and Reduction Potentials of Transient Free Radicals1," *J. Am. Chem. Soc*, vol. 110, pp. 132–137, 1988.

[30] C. P. Andrieux, I. Gallardo, and J.-M. Savéant, "Outer-Sphere Electron-Transfer Reduction of Alkyl Halides. A Source of Alkyl Radicals or of Carbanions? Reduction of Alkyl Radicals," *J. Am. Chem. Soc*, vol. 111, pp. 1620–1626, 1989.

[31] B. Meschi Amoli, J. Trinidad, A. Hu, Y. N. Zhou, and B. Zhao, "Highly electrically conductive adhesives using silver nanoparticle (Ag NP)-decorated graphene: the effect of NPs sintering on the electrical conductivity improvement," *J. Mater. Sci. Mater. Electron.*, vol. 26, no. 1, pp. 590–600, 2014.

[32] V. K. Rao, Venkata Abhinav, Karthik, P. S., and S. P. Singh, "Conductive silver inks and their applications in printed and flexible electronics," *RSC Adv.*, vol. 5, no. 95, pp. 77760–77790, 2015.

[33] G. Vandevenne *et al.*, "A study on the thermal sintering process of silver nanoparticle inkjet inks to achieve smooth and highly conducting silver layers," *Phys. Status Solidi*, vol. 7, p. n/a-n/a, 2016.

[34] M. Grouchko, A. Kamyshny, C. F. Mihailescu, D. F. Anghel, and S. Magdassi, "Conductive inks with a 'built-in' mechanism that enables sintering at room temperature," *ACS Nano*,

vol. 5, no. 4, pp. 3354–3359, 2011.

[35] A. Bard, R. Parsons, and J. Jordan, *Standard potentials in aqueous solution*, 1st ed. International Union of Pure and Applied Chemistry, 1985.

[36] M. K. Sharma, R. D. Buchner, W. J. Scharmach, V. Papavassiliou, and M. T. Swihart, "Creating Conductive Copper-Silver Bimetallic Nanostructured Coatings Using a High Temperature Reducing Jet Aerosol Reactor," *Aerosol Sci. Technol.*, vol. 47, no. 8, pp. 858–866, 2013.

[37] S. Gamerith, A. Klug, H. Scheiber, U. Scherf, E. Moderegger, and E. J. W. List, "Direct ink-jet printing of Ag-Cu nanoparticle and Ag-precursor based electrodes for OFET applications," *Adv. Funct. Mater.*, vol. 17, no. 16, pp. 3111–3118, 2007.

[38] G. Gupta *et al.*, "Pt Diffusion Dynamics for the Formation Cr-Pt Core-Shell Nanoparticles," *Langmuir*, vol. 31, no. 24, pp. 6917–6923, 2015.

[39] M. Green and P. O'Brien, "The preparation of organically functionalised chromium and nickel nanoparticles," *Chem. Commun.*, pp. 1912–1913, 2001.

[40] K. M. Koczkur, S. Mourdikoudis, L. Polavarapu, and S. E. Skrabalak, "Polyvinylpyrrolidone (PVP) in nanoparticle synthesis," *Dalt. Trans.*, vol. 44, pp. 17883–17905, 2015.

[41] M. Luo, Y. Hong, W. Yao, C. Huang, Q. Xu, and Q. Wu, "Facile removal of polyvinylpyrrolidone (PVP) adsorbates from Pt alloy nanoparticles," *J. Mater. Chem. A*, vol. 3, no. 6, pp. 2770–2775, 2015.

[42] A. Nemamcha, H. Moumeni, and J. L. Rehspringer, "PVP Protective mechanism of

palladium nanoparticles obtained by sonochemical process," *Phys. Procedia*, vol. 2, no. 3, pp. 713–717, 2009.

[43] T. Teranishi and M. Miyake, "Size Control of Palladium Nanoparticles and Their Crystal Structures," *Chem. Mater.*, vol. 10, no. 2, pp. 594–600, 1998.

[44] F. Bonet, V. Delmas, S. Grugeon, R. Herrera Urbina, P. Y. Silvert, and K. Tekaia-Elhsissen, "Synthesis of monodisperse Au, Pt, Pd, Ru and Ir nanoparticles in ethylene glycol," *Nanostructured Mater.*, vol. 11, no. 8, pp. 1277–1284, 1999.

[45] Y. Borodko, H. Sook Lee, S. Hoon Joo, Y. Zhang, and G. Somorjai, "Spectroscopic Study of the Thermal Degradation of PVP-Capped Rh and Pt Nanoparticles in H 2 and O 2 Environments."

[46] W. Niu *et al.*, "Seed-mediated growth of nearly monodisperse palladium nanocubes with controllable sizes," *Cryst. Growth Des.*, vol. 8, no. 12, pp. 4440–4444, 2008.

[47] N. Su *et al.*, "The facile synthesis of single crystalline palladium arrow-headed tripods and their application in formic acid electro-oxidation," *Chem. Commun.*, vol. 51, no. 33, pp. 7195–7198, 2015.

[48] I. Puigdomenech, "Hydra/Medusa." Stockholm, 2010.

[49] Y. Wang, T. Herricks, and Y. Xia, "Single crystalline nanowires of lead can be synthesized through thermal decomposition of lead acetate in ethylene glycol," *Nano Lett.*, vol. 3, no. 8, pp. 1163–1166, 2003.

[50] S. Özkar and R. G. Finke, "Palladium(0) Nanoparticle Formation, Stabilization, and Mechanistic Studies: $Pd(acac)_2$ as a Preferred Precursor, $[Bu_4N]_2HPO_4$ Stabilizer, plus

the Stoichiometry, Kinetics, and Minimal, Four-Step Mechanism o," *Langmuir*, vol. 32, no. 15, pp. 3699–3716, 2016.

[51] S. E. Skrabalak, B. J. Wiley, M. Kim, E. V. Formo, and Y. Xia, "On the polyol synthesis of silver nanostructures: Glycolaldehyde as a reducing agent," *Nano Lett.*, vol. 8, no. 7, pp. 2077–2081, 2008.

[52] P. Chokratanasombat and E. Nisaratanaporn, "Preparation of ultrafine copper powders with controllable size via polyol process with sodium hydroxide addition," *Eng. J.*, vol. 16, no. 4, pp. 39–46, 2012.

[53] M. Y. Sen and J. E. Puskas, "Green polymer chemistry: Telechelic poly(ethylene glycol)s via enzymatic catalysis," *Am. Chem. Soc. Polym. Prepr. Div. Polym. Chem.*, vol. 49, no. 1, pp. 487–488, 2008.

[54] B. Schmid, M. Döker, and J. Gmehling, "Esterification of ethylene glycol with acetic acid catalyzed by Amberlyst 36," *Ind. Eng. Chem. Res.*, vol. 47, no. 3, pp. 698–703, 2008.

[55] V. L. Nguyen, D. C. Nguyen, H. Hirata, M. Ohtaki, T. Hayakawa, and M. Nogami, "Chemical synthesis and characterization of palladium nanoparticles," *Adv. Nat. Sci. Nanosci. Nanotechnol.*, vol. 1, no. 3, p. 035012, 2010.

[56] T. D. Donnelly *et al.*, "Using ultrasonic atomization to produce an aerosol of micron-scale particles," *Rev. Sci. Instrum.*, vol. 76, no. 11, pp. 1–10, 2005.

[57] S. Binder, M. Glatthaar, and E. Rädlein, "Analytical investigation of aerosol jet printing," *Aerosol Sci. Technol.*, vol. 48, no. 9, pp. 924–929, 2014.

[58] OPTOMEC, "Aerosol Jet ® Printed Electronics Overview."

[59] S. K. Tam, K. Y. Fung, G. S. H. Poon, and K. M. Ng, “Product Design: Metal Nanoparticle-Based COnductive Inkjet Inks,” *AIChE J.*, vol. 62, no. 8, pp. 2740–2753, 2016.

[60] K. Vanheusden *et al.*, “Metal Nanoparticle Compositions,” 2006/0189113A1, 2006.

[61] J. Park and J. Moon, “Control of Colloidal Particle Deposit Patterns within Picoliter Droplets Ejected by Ink-Jet Printing.”

[62] N. Nalajala, W. F. Gooty Saleha, B. P. Ladewig, and M. Neergat, “Sodium borohydride treatment: a simple and effective process for the removal of stabilizer and capping agents from shape-controlled palladium nanoparticles.,” *Chem. Commun. (Camb).*, pp. 9365–9368, 2014.

[63] J. Chou, M. McAllister, and P. Schottland, “Aerosol jet printable metal conductive inks, glass coated metal conductive inks and uv-curable dielectric inks and methods of preparing and printing the same,” US20140035995A1.

[64] P. Salami, P. Liu, C. G. Allen, N. Chopra, and K. I. Halfyard, “Silbernanopartikeltinte Silver nanoparticle ink.” Google Patents, 2017.

[65] J. P. Novak and L. Yunjun, “Surface-Modified Nanoparticle Ink For Photovoltaic Applications,” 2013/0017647, 2013.

[66] Y. J. Du, M. Damron, G. Tang, H. Zheng, C. J. Chu, and J. H. Osborne, “Inorganic / Organic Hybrid Coatings for Aircraft Aluminum Alloy Substrates Corrosion Inhibitors - Current Corrosion Inhibitors - Future Sol Gel The Sol-Gel Process Durability,” *Prog. Org. Coatings*, vol. 41, pp. 226–232, 2001.

[67] T. Ishizaka, S. Muto, and Y. Kurokawa, “Nonlinear optical and XPS properties of Au and

Ag nanometer-size particle-doped alumina ® lms prepared by the sol ± gel method," vol. 190, no. April, pp. 385–389, 2001.

[68] M. Guglielmi, G. Kickelbick, and A. Martucci, "Sol-Gel Nanocomposites."

[69] V. Chiola, J. E. Ritsko, and C. D. Vanderpool, "No Title," 3, 1971.

[70] H. Uchihashi, N. Tohge, and T. Minami, "Preparation of Amorphous Al2O3 Thin Films from Stabilized Al-Alkoxides by the Sol-Gel Method," *Nippon Seramikkusu Kyokai Gakujutsu Ronbunshi*, vol. 97, no. 1123, pp. 396–399, 1989.

[71] H. Schmidt, "New type of non-crystalline solids between inorganic and organic materials," *J. Non. Cryst. Solids*, vol. 73, no. 1–3, pp. 681–691, 1985.

[72] E. J. Kappert, D. Pavlenko, J. Malzbender, A. Nijmeijer, N. E. Benes, and P. A. Tsai, "Formation and prevention of fractures in sol–gel-derived thin films," *Soft Matter*, vol. 11, no. 5, pp. 882–888, 2015.

[73] C. J. Brinker, "Chemical Solution Deposition of Functional Oxide Thin Films," 2013, pp. 233–261.

[74] Z. Chen, R. Burtovyy, K. G. Kornev, I. Luzinov, and F. Peng, "Dense and crack-free mullite fi lms obtained from a hybrid sol – gel / dip-coating approach," pp. 1665–1673, 2017.

[75] B. Hu, E. Jia, B. Du, and Y. Yin, "A new sol-gel route to prepare dense Al 2 O 3 thin films," *Ceram. Int.*, vol. 42, no. 15, pp. 16867–16871, 2016.

[76] Y. Castro, A. Duran, J. J. Damborenea, and A. Conde, "Electrochemical behaviour of silica basic hybrid coatings deposited on stainless steel by dipping and EPD," *Electrochim. Acta*, vol. 53, no. 20, pp. 6008–6017, 2008.

[77] T. Wang, J. Pu, C. Bo, and L. Jian, “Sol-gel prepared Al2O3 coatings for the application as tritium permeation barrier,” *Fusion Eng. Des.*, vol. 85, no. 7–9, pp. 1068–1072, 2010.

[78] a. R. Olszyna, P. Marchlewski, and K. J. Kurzydłowski, “Sintering of high-density, high-purity alumina ceramics,” *Ceram. Int.*, vol. 23, no. 4, pp. 323–328, 1997.

[79] D. Wang and G. P. Bierwagen, “Sol-gel coatings on metals for corrosion protection,” *Prog. Org. Coatings*, vol. 64, no. 4, pp. 327–338, 2009.

[80] C. Jing, X. Zhao, and Y. Zhang, “Sol-gel fabrication of compact, crack-free alumina film,” *Mater. Res. Bull.*, vol. 42, no. 4, pp. 600–608, 2007.

[81] J. J. Ebelmen, “No Title,” *Ann. Chem. Phys.*, vol. 5, p. 199, 1842.

[82] R. K. Datta and R. Roy, “LiAI,O,” *J. Am. Ceram. Soc.*, vol. 46, no. 8, pp. 388–390, 1963.

[83] S. Lamouri *et al.*, “Control of the γ-alumina to α-alumina phase transformation for an optimized alumina densification,” *Boletín la Soc. Española Cerámica y Vidr.*, vol. 56, no. 2, pp. 47–54, Mar. 2017.

[84] L. Yang, *Materials Characterization: Introduction to Microscopic and Spectroscopic Methods*, 2nd ed. Weinhiem, Germany: Wiley-VCH, 2013.

[85] B. Ravel, E. E. Carpenter, and V. G. Harris, “Oxidation of iron in iron/gold core/shell nanoparticles,” *J. Appl. Phys.*, vol. 91, no. 10 I, pp. 8195–8197, 2002.

Appendix A Supplementary Info

A.1 Synthesis Screening

A large part of the work in this thesis was to screen techniques that could be suitable for the creation of PdCr13 alloy nanoparticles.

A.1.1 Materials

The following materials were employed in the screening process. The sodium citrate dihydrate and tannic acid ACS were sourced from Alpha Aesar. Chromium nitrate nonahydrate 99.99%, palladium nitrate hydrate 40% palladium basis, chromium acetate hydroxide, 1-methoxy-2-propanol, α-terpineol, hydrazine hydrate, ethylenediaminetetraacetic acid (EDTA), and glacial acetic acid were sourced from Sigma Aldrich.

A.1.1.1 Sodium Citrate Reduction

At the onset of the project the reduction chemical proposed for making PdCr13 particles was sodium citrate. The reduction pathways have been well established for the likes of silver and gold, where it serves as both a reducing agent and a stabilizer for the particles.

A typical synthesis followed:

1. Heat 100 mL of distilled water to 80˚C
2. Add 226 mg of palladium nitrate nonahydrate and 120 mg chromium nitrate to solution.
3. Rapidly add 565 mg sodium citrate and 16 mg tannic acid to solution

4. Heat for 1 hour
5. Centrifuge to collect particles

Figure 39 shows the first attempts at printing with such a formulation. The brown color is indicative of the tannic acid that was included as a control reagent to the chemical reduction. The printed ink existed as a mixture of reduced palladium nanoparticles and chromium, sodium, and organic salt. This is because of two properties of the ink. The first being that according to Equation 26 for this reaction to be favorable the citrate ion must exist in concentrations 3 billion times greater than the concentration of chromium salts. The second is that the sodium salts in the reaction are difficult to separate out from the ink. Remaining sodium salts will cause electrical and structural interference at the intended high temperatures.

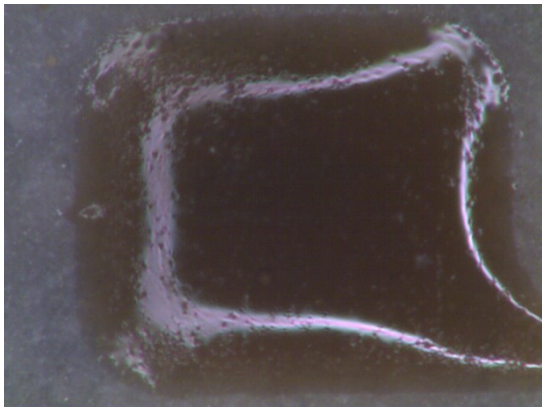

Figure 39 Original print of sodium citrate formulations

When heated the salt forms a matrix with the nanoparticles within it. If there is too much salt like in Figure 40 the palladium particles are so sparse that they do not create a connected pathway required for conductivity. A connected network of particles is said to have reached the percolation threshold.

Throughout the GE project the sodium citrate route was codeveloped alongside alternative synthesis routes. That work is outside the scope of this thesis.

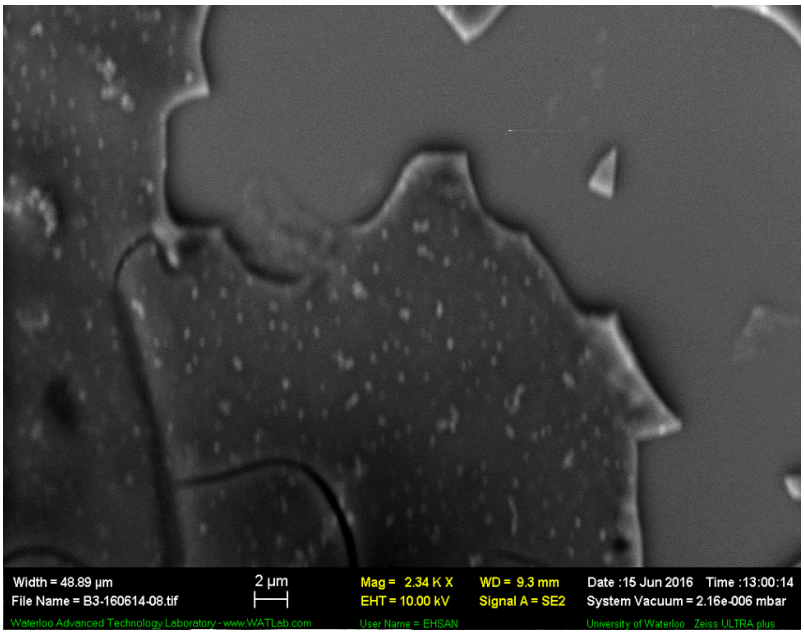

Figure 40 Excess contaminants found in the citrate reduction route

A.1.1.2 Hydrazine Reduction

Following the trend in increased chemical potential, hydrazine was the next reducing agent screened. Hydrazine decomposes into ammonia, hydrogen and nitrogen. Hydrazine has a reduction potential of -0.33V. Following The concentrations for the reaction being favorable is approximately 10 million times more concentrated than the chromium ion. Still the hydrazine reaction was good to investigate as the hydrazine reducing agent proved to be the ideal reducing agent for the palladium salts.

Figure 41 is an image of the particles produced by the hydrazine reaction. As hydrazine was a stronger reducing agent the particle size of the palladium nanoparticles formed was smaller than

that of the sodium citrate. However on a sample that targeted 90% chromium content only 10 % of the chromium was able to be detected by EDS. Such a low percentage is probably because the chromium existed as either a hydroxide or an oxide contaminant in the ink. The contaminating chromium species formed as a layer on the outside of the particles. A typical shell of the contaminants is imaged in Figure 42.

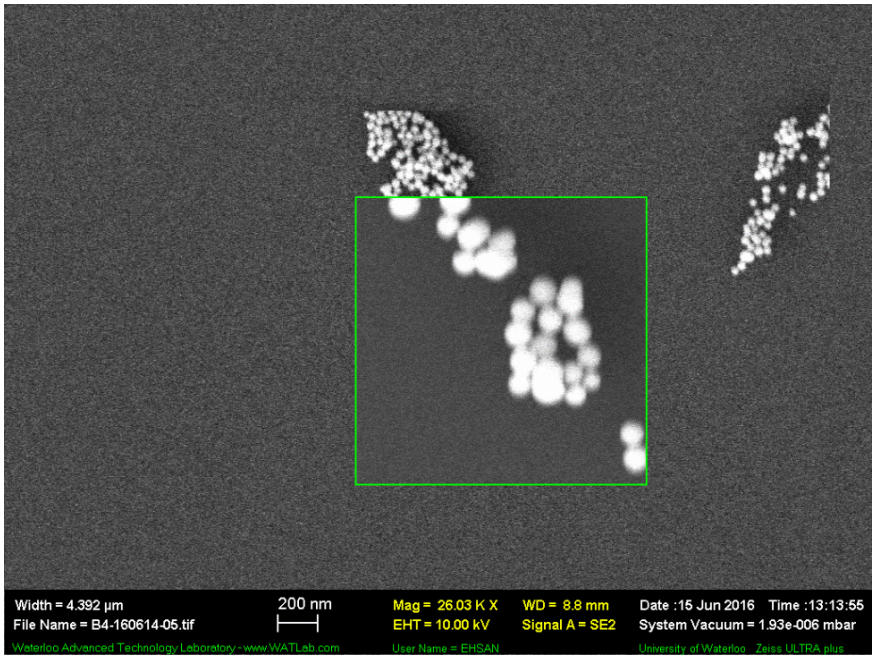

Figure 41 Nanoparticles produced by hydrazine reaction. Target of 10% palladium, actual 90%.

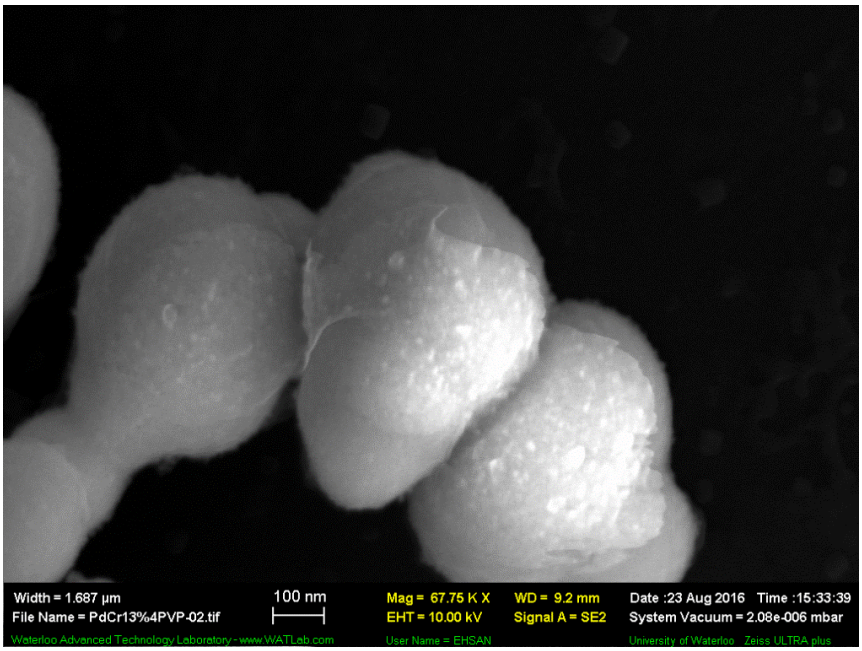

Figure 42 Hydrazine reduced nanoparticles with chromium oxide shell

The hydrazine also comes as a hydrate in water, so that in adding small traces of the hydrazine water was introduced into the system.

A.1.1.3 Sodium Borohydride Reduction

In comparison the sodium borohydride reducing agent has more probable thermodynamics than the previous reducing agents described. In the work here the reducing agent had a few issues with its implementation. The compound is typically reactive and decomposes rapidly in alcohols and water. Typically sodium borohydride was added directly to the reaction as a solid to try and mitigate these issues.

For a theoretically possible reduction of chromium salts the concentration has to be thirty thousand times greater than the salt concentration. When the reaction produces nanoparticle chromium in

solution the solution is a dark brown color, however these particles are only obtained after removing the side products formed during the reaction. As in

Figure 43 the sodium borohydride can also reduce the solvent ethylene glycol or if water is present or added to the reaction the formation of the chromium hydroxide still dominates over that of the chromium metal formation. As with Gupta et al. [38] I've found that this reaction produces chromium oxide in greater concentrations that the pure chromium metal formed. With the yield being low and the side reactions being prominent the sodium borohydride reaction failed to provide the chromium nanoparticles that could be used to create PdCr13.

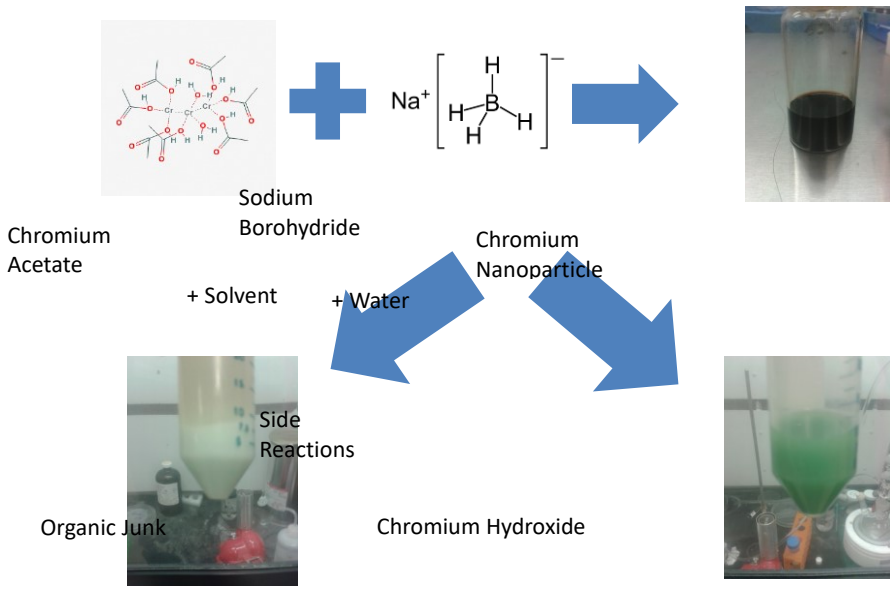

Figure 43 Sodium borohydride reaction overview

A.1.1.4 N-Butyl Lithium Reduction

N-butyl lithium was the most powerful reducing agent that was attempted to be used for the reduction of chromium. N-butyl lithium essentially provided a carbocation to the solution, that is

a carbon atom with an extra electron. The carbon atom holding a negative charge is extremely unstable and will give that electron to almost any substance around it. The compound was difficult to work with as it had to be used in inert atmospheres without oxygen or moisture as it would auto ignite if exposed.

Again the same issues with the sodium borohydride were experienced. The reactions had many side products as the n-butyl lithium also was reducing the solvent. Part of the problem was that the chromium acetate required polar solvents to suspend the salt while the n-butyl lithium was only stable in non-polar solvents leading to immiscibility of the compounds.

Trace chromium nanoparticles were produced with questionable quality and purity, as attempts at making PdCr13 with the as produced particles did not produce the appropriate chromium contents or conductivity in the final inks.

A.2 Characterization information

A.2.2 X-ray Techniques

X-Ray processes are a way to identify and quantify chemical elements present in the sample. They do this by examining characteristic emission of x-rays from the elements when excited by a high energy source. These emissions come from the energy difference between an electron's excited and ground state in a specific element.

The emitted x-rays have their characteristic properties dependent on the path the electron takes to decay in the atom. These paths are typically denoted by K, L, and M lines in nomenclature.

These letters denote the principle quantum number that the electron is decaying to with K, L and M being 1, 2 and 3 respectively. These letters are often suffixed with a Greek letters α,β,γ denoting decreasing observed intensity. Therefore the most common line Kα means the x-ray produced from the decay of an electron in the 2p shell to the 1s shell. The allowed spectra and their intensities follow quantum selection rules.

These emitted x-rays can be detected and interpreted in two different manners. The equipment can measure the wavelength or energy of the emitted x-ray. Techniques that measure the wavelength of the x-ray are cataloged as wavelength dispersive spectroscopy (WDS) techniques and ones that measure the energy are called energy dispersive spectroscopy (EDS) techniques. Typically WDS techniques are more specialized as one can filter the wavelengths of interest from a sample where-as EDS techniques grab the entire broad spectra of emission from the sample.

Two pieces of equipment are commonly used for these techniques, X-ray Fluorescence spectrometers (XRF) and electron microscopes. The two machines differ in their energy sources that they use to excite the x-ray emission. For XRF machines the energy source is an x-ray where the response is the "fluorescence". This x-ray source is by necessity quite broad and cannot be focused as electron sources may be. In the efforts presented here the focus is on electron microscopy.

A.2.2.5 Energy dispersive analysis

EDS analysers employ the ability of a Si(Li) diode to sample the entire spectrum of energy at the same time. As a result the EDS technique is a fast and cheap method for elemental analysis. The lightest element that EDS systems can detect is oxygen. One of the set-backs to this technique is

that the diode must be separated from the rest of the system by a beryllium window. This window will absorb some x-rays.

In addition to the beryllium window there is also a material filter on the incoming x-rays that complicates the system. This filter is required because earlier systems typically produced too many photons for the detectors to correctly interpret due to a saturation of electron-hole pairs in the diode. These filters create secondary fluorescence from the characteristic radiation of the filter and limit the energy of the incoming x-rays.

The EDS technique samples the entire spectra of the x-ray emission from the sample. As such there is significant noise in the sample from the background radiation that is not filtered out as is the case with WDS. The direct result is that the resolution of the EDS system is about 10 times lower than the WDS system. These problems with the EDS system typically mean that the technique is limited to making qualitative analysis on samples.

A.2.3 Electron-Microscopy enabled Energy Dispersive Spectroscopy

Since EDS technology is so accessible and compact it is a common accessory to electron microscopes. The difference between EM EDS and XRF EDS is that the sample is excited by a focused electron beam rather than x-rays. This allows for microscopic analysis and mapping of a sample. One important caveat to this behaviour is that the area sampled by this technique is not the same area as is being imaged by the electron beam spot side. The x-rays generated in the sample come from a pear-shaped region under the electron beam from the excited material. The higher the density of the material the lower volume this region will be. The best approximation for the emission volume for this volume (R) is given by[84]:

$$R = \frac{0.064(E_o^{1.7} - E_{ex}^{1.7})}{\rho}$$ Equation 31

Where E_o is the acceleration voltage of the electron beam, E_{ex} is the characteristic X-ray for the element, and ρ is the density. The immediate implication of this formula is that for elements with a lower characteristic energy will have a larger volume that is sampled than others.

A.2.4 X-ray Based Quantitative Elemental Analysis

Quantitative analysis based on x-ray techniques rely on comparing the area underneath each x-ray emission peak for the sample. These ratios are called the relative intensities (I_R). The weight fraction (C) can be calculated in general by:

$$C = MKI_R$$ Equation 32

K is an instrumental factor related to the excitation source, alignment of the specimen and detector as well as the detector`s sensitivity to the radiation. M is a material factor containing information about the different interactions between the elements in the specimens.

Leng points out that the M factor has three main components: primary absorption, secondary absorption and secondary fluorescence [84]. Primary absorption is the materials ability to absorb the incoming radiation for excitation. When analyzing PdCr13 palladium will inherently have a larger primary absorption factor than the chromium. This effect however will be greatly offset by secondary fluorescence. Secondary fluorescence occurs when elements in the sample can be excited by the emission from other elements. The emission energy of palladium, which is ~21 keV, is more than sufficient to excite the chromium in the sample which has an energy of ~5.4 keV. As

a general rule the excitation energy should be 3-5 times higher than the characteristic emission. Secondary absorption is the factor relating to the materials ability to block the emission from the elements before they escape to the detector.

The most common way to account for the M factor is to use a reference sample of known concentration that is comparable to the sample that we are analyzing. For our purposes this would require a target that is a 13% chromium alloy in palladium.

The K factor can be adjusted for by keening the measurement parameters the same from sample to standard. This means that the acceleration voltage for electron microscope, angle between sample and detector and intensity at the detector should be kept constant.

When standards are not available in electron microscope techniques often standardless quantitative analysis can be employed. The standardless technique uses the library of information on the pure elements and their relative intensities to iteratively determine the sample's composition. This technique is good for compositions that do not have significant issues with secondary absorption or fluorescence. There are a few easy ways to determine the aptness of this technique such as looking at the change in analysis results between the different x-ray lines, changing incident energy or count rates.

A.2.5 Thermal Gravimetric Analysis (TGA)

TGA is essentially scientific thermal degradation of a given sample. The two common components are a delicate weigh scale and a furnace with a controlled atmosphere. The furnace can control the heating rate of the material sample up to a desired temperature. The scale then monitors any weight

change due to the volatilization of the compound or the gain from reactions with the gas environment.

A.2.6 Preparation of Core Shell Nanoparticles in Literature.

The overall reaction is graphically displayed in Figure 44 below. The first chemical species in their synthesis to introduce is the chelating agent, [2,2'-bipyridine]-5-diazonium (D-BiPy). The reaction was carried out such that the metal species were at a 1:1 molar ratio with 30 µmols of chromium. The chelating agent is present to stabilize the chromium nanoparticles with an organic layer and provide binding sites for platinum localization. In the reaction there is one chelating agent molecule for every metal atom. The chromium source is derived from $CrCl_3$ pentahydrate. To the 30 µmols of chromium 20 mmols of sodium borohydride was added as a reducing agent. The sodium borohydride leaves sodium contaminants in solution but is a stable strong reducing agent. After reaction completion the platinum was added in the form of dichloro(1,5-cyclooctadiene) platinum(II). The organically complexed platinum is soluble in the ethanol solvent and slightly retards the reduction of the precursor.

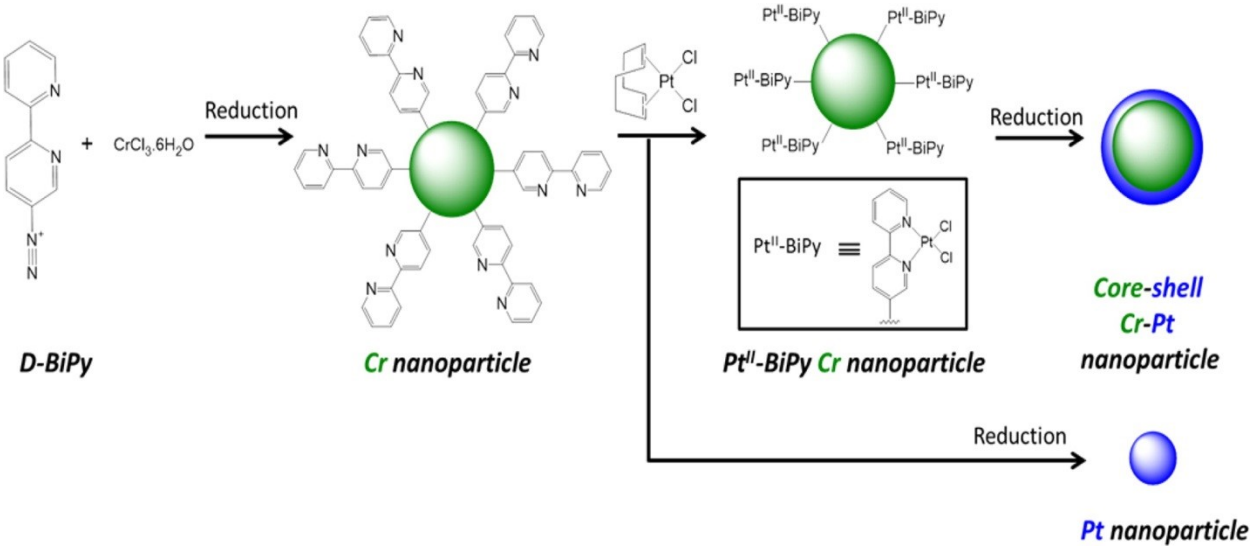

Figure 44 Gupta et al.'s synthesis procedure

The produced nanoparticles were fully characterized by EDX, STEM, XRD, and XPS. EDX (EDS) was used to characterize the pure chromium nanoparticles as an initial qualitative elemental analysis. The elemental analysis revealed that even at this stage the chromium nanoparticles contained significant oxygen contents. XRD analysis revealed the presence of FCC structures typically attributed to noble metal formation and determined the crystal size between grain boundaries to be 2.3 nm. XPS, which is a surface sensitive technique that penetrates at a maximum of 10 nm [84], determined qualitatively that chromium, Cr_2O_3, N, Pt, and $Pt(OH)_2$ was present in the sample. The final analysis technique of STEM was employed to confirm the existence of the core-shell nanoparticles, the different elements will have a different contrast in the analysis technique. Using this contrast one can tell the exact morphology of the particles. It was found that intensity profiles most likely correspond to a structure where a Pt-Cr alloy is encapsulated by a chromium oxide-platinum mixture. Even when the shell is properly deposited there runs the risk that shells are not formed over localized growth into an egg-yolk structure [85].

A.2.7 Chromium Materials

The sourced particles were produced by a wire explosion technique where a thin wire of the material is drawn and a large current is pushed through the thin wire. The rapid heating of the wire causes the wire to fragment into nanoparticles. These particles are advertised as 40 nm large with a cubic structure as depicted in Figure 45. These particles are almost too large to cover with the required palladium to reach a weight percentage of palladium of 83%. If all the palladium goes to the shell of such a particle the total size of the particle is more than 100 nm which makes printing with these particles difficult as they clog the system and settle out of inks much easier.

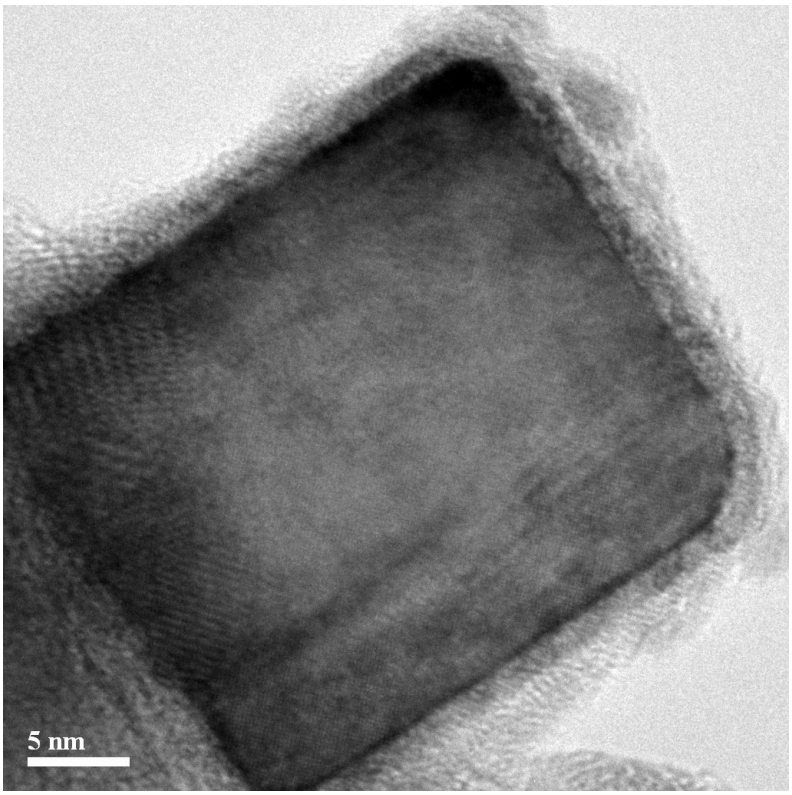

Figure 45 TEM image bare commercial chromium nanoparticle

Figure 45 shows the basic structure of these particles. They are purchased already capped with PVP which can be seen at the edges of the cube. The cubes of chromium have a regular crystal structure.

A.3 Supplementary I-V Curves

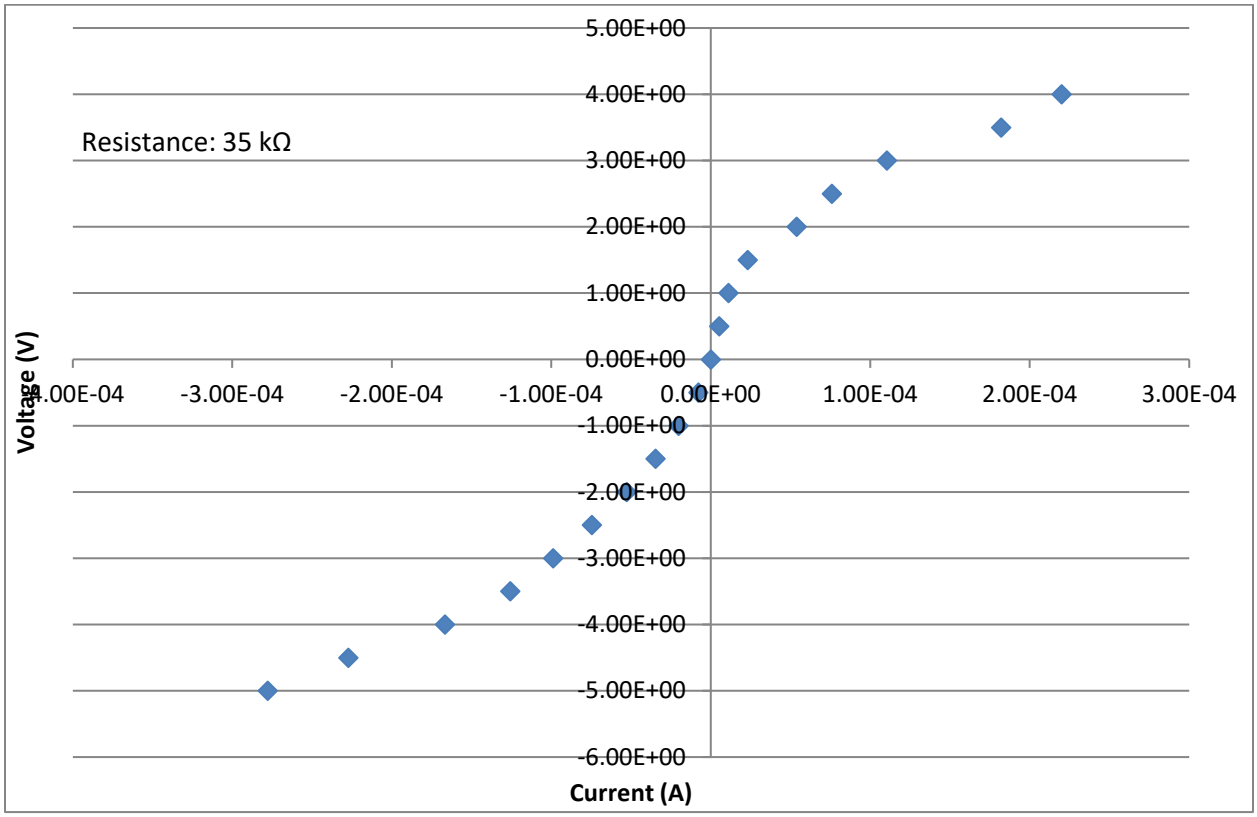

Figure 46 A low resistance non-linear resistive response

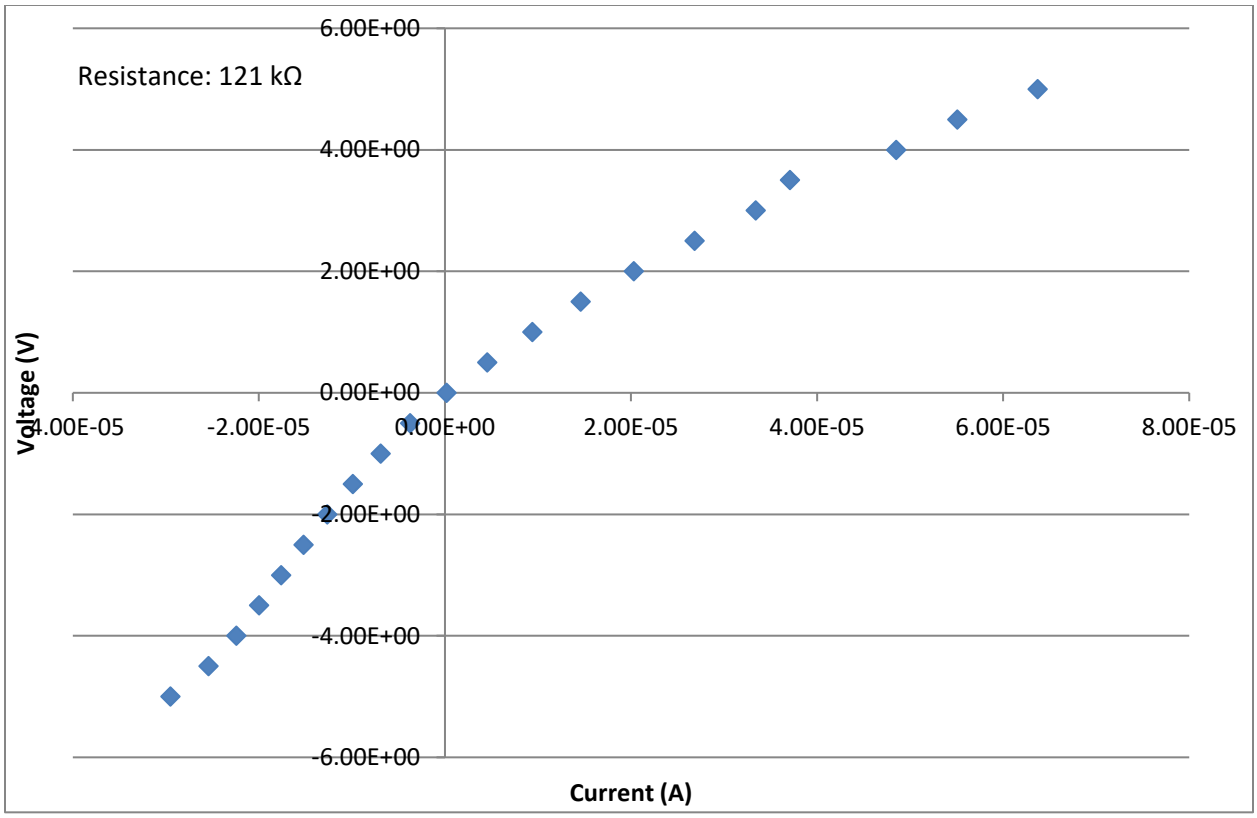

Figure 47 Changes in linearity depending on polarity

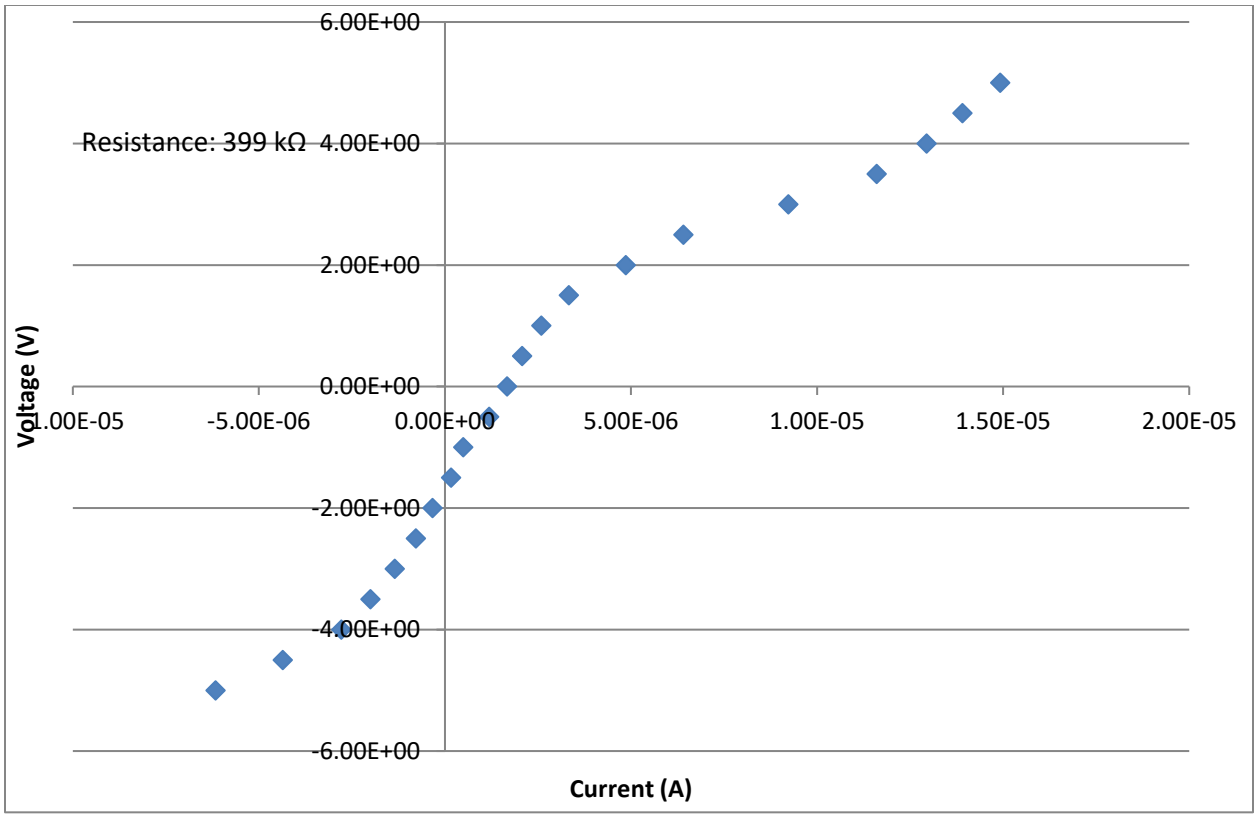

Figure 48 Non-linear break down when excited above 2V.